

# A review of the processing, composition, and temperature-dependent mechanical and thermal properties of dielectric technical ceramics

Daithí de Faoite · David J. Browne ·  
Franklin R. Chang-Díaz · Kenneth T. Stanton

Received: 3 August 2011 / Accepted: 17 November 2011 / Published online: 8 December 2011  
© Springer Science+Business Media, LLC 2011

**Abstract** The current review uses the material requirements of a new space propulsion device, the Variable Specific Impulse Magnetoplasma Rocket (VASIMR<sup>®</sup>) as a basis for presenting the temperature-dependent properties of a range of dielectric ceramics, but data presented could be used in the engineering design of any ceramic component with complementary material requirements. A material is required for the gas containment tube (GCT) of VASIMR<sup>®</sup> to allow it to operate at higher power levels. The GCT's operating conditions place severe constraints on the choice of material. An electrically-insulating material is required with a high-thermal conductivity, low-dielectric loss factor, and high-thermal shock resistance. There is a lack of a representative set of temperature-dependent material property data for materials considered for this application and these are required for accurate thermo-structural modelling. This modelling would facilitate the selection of an optimum material for this component. The goal of this article is to determine the best material property data values for use in the materials selection and design of such components. A review of both experimentally and theoretically determined temperature-dependent and room temperature properties of several materials has been undertaken. Data extracted are presented by property. Properties reviewed are density, Young's, bulk and shear moduli, Poisson's ratio, tensile, flexural and compressive strength, thermal conductivity,

specific heat capacity, thermal expansion coefficient, and the factors affecting maximum service temperature. Materials reviewed are alumina, aluminium nitride, beryllia, fused quartz, sialon, and silicon nitride.

## Introduction

The Variable specific-impulse magnetoplasma rocket [1] (VASIMR<sup>®</sup>) is an advanced electric propulsion rocket pioneered at the NASA Advanced space propulsion laboratory, and currently being developed by the Ad Astra Rocket Company, Houston, Texas. It uses strong, shaped magnetic fields to contain and direct a high-power plasma for high-specific impulse propulsive thrust. The plasma is created using helicon electromagnetic waves [2] in what is thereby known as the helicon section of the engine. A gas containment tube (GCT) is used in this helicon section to contain the neutral gas prior to ionization and to ensure physical separation between the neutral gas and the helicon antenna. The helicon plasma generation process is not completely efficient and results in large amounts of the input RF-energy being lost as waste heat. This heat is deposited on the inner surface of the GCT by the processes of volumetric radiation, Bohm diffusion, and collisions from high-temperature neutral atoms [3]. Excessive temperatures in the helicon section from this waste heat may pose a problem, not only to the structural integrity of the GCT, but also to the operation of the superconducting magnets required to contain the plasma [4].

The heat flux from the plasma is not only large but is also non-uniformly distributed over the inside surface of the GCT, and a material used for this application must be capable of dissipating this waste heat to a heat exchanger or radiator. Peak heat loads have been observed downstream of and directly under the helicon antenna [5].

D. de Faoite · D. J. Browne · K. T. Stanton (✉)  
School of Mechanical and Materials Engineering, University  
College Dublin, Belfield, Dublin 4, Ireland  
e-mail: Kenneth.Stanton@ucd.ie

F. R. Chang-Díaz  
Ad Astra Rocket Company, 141 W. Bay Area Blvd.,  
Webster, Houston, TX 77598, USA

The non-uniformity of the heat deposition leads to high-localized temperatures and large temperature gradients in the GCT walls. Furthermore, during operation, the RF power may be cycled on and off repeatedly, inducing cyclic thermal stresses in the components of the engine.

The conditions under which the material must operate place stringent constraints on the materials that can be used. A fully dense material is required with high strength, high-thermal conductivity, and high-thermal shock resistance. High electrical resistivity and low dielectric loss factor are also required in order to minimize dielectric heating from the helicon antenna. The selection of materials for this application has many similarities to the constraints imposed in the selection of materials for microwave and RF-waveguide windows, radomes for missiles and supersonic aircraft, dielectric components in ion engines and hall thrusters, and dielectric heat spreaders in electronics.

Fused quartz has been used successfully as the GCT material in previous VASIMR<sup>®</sup> prototype engines [2, 6]. Fused quartz has also been used in other large diameter helicon plasma sources [7], and widely used as a gas containment tube material in helicon plasma sources for plasma-assisted coating and sputtering applications [8], (where commonly referred to as a ‘discharge tube’). Pyrex<sup>®</sup> has also been used as a GCT material in low power helicon plasma sources [9, 10]. Borosilicate glass has been used as the material in a small-diameter plasma discharge tube [11]. Alumina and sapphire have also been used as plasma containment tube materials [12–15]. However, the current 200 kW VASIMR<sup>®</sup> prototype poses a significantly greater challenge than that faced by most plasma generation sources, due to the large physical size and very large heat fluxes. This prototype rocket will have approximately twice the total electrical power input of the previous prototype in order to increase the amount of thrust generated by the rocket. Selection of a suitable material for the GCT of the prototype is thus required. The candidate materials considered in this review are alumina (Al<sub>2</sub>O<sub>3</sub>), aluminium nitride (AlN), beryllia (BeO), sialon, and silicon nitride (Si<sub>3</sub>N<sub>4</sub>).

When selecting a material for such an application, or when modelling or optimising such a component, the designer requires dependable representative material property data. During the detailed design process it is best to conduct a series of standardised tests on the chosen material, or selection of materials, from different manufacturers in order to verify their properties. However, it is usually impractical at the outset of the design process to test a vast number of different material types from different vendors. The focus of this paper is to find a set of representative, self-consistent values of material properties for several high performance commercially available ceramics being considered for use for the VASIMR<sup>®</sup> GCT, which may be used for such modelling and preliminary selection.

Values of thermophysical properties are widely taken as constants with respect to temperature in design, despite the clear variation in some properties with temperature. For hardware components which must dissipate large amounts of waste heat, such as the VASIMR<sup>®</sup>, temperature-dependent material property data are critical for component design, simulation, and materials selection, and to allow accurate prediction of the effects of thermal shock and fatigue, and the component’s susceptibility to thermal stress-induced failure. Variations in ceramic material properties with temperature increases above room temperature are typically detrimental from a design point of view; with increases in temperature causing decreases in strength, moduli, thermal conductivity, electrical resistivity, and increases in thermal expansion coefficient, and dielectric loss factor. Room temperature material property values are useful for identifying a number of different materials that could be feasibly used, but failure to use temperature-dependent data in simulations can lead to inadequate designs, due to the simultaneous deterioration of many properties.

The focus of this analysis is on literature-derived data for commercially available material grades. It is not intended to be an exhaustive review of all existing data, but instead a representative summary of typical temperature-dependent data. Property data, where available are widely scattered, especially in the cases of fused quartz and sialon. Temperature-dependent data are not available for every material property for each material, but have been presented where possible. Comparatively limited data are available for Weibull analyses [16] of ceramic strengths in the literature, especially at elevated temperatures. Hence, strength data are presented only in terms of mean values. Representative thermal and mechanical property data for alumina, aluminium nitride, beryllia, sialon, and silicon nitride are presented, along with data for fused quartz. The material properties considered are listed in Table 1. Points plotted in each graph represent data-points from the original reports; dashed lines are a guide to the reader’s eye. Solid lines represent data presented in the form of curves rather than discrete data-points in the original reports.

**Table 1** Material properties considered

Mechanical	Thermal
Density	Thermal conductivity
Young’s modulus	Specific heat capacity
Bulk modulus	Thermal expansion coefficient
Shear modulus	
Poisson’s ratio	
Tensile strength	
Flexural strength	
Compressive strength	

**Table 2** Summary of material properties considered

	Alumina	Aluminium nitride	Beryllia	Fused quartz	Sialon	Silicon nitride
Processing	Sintered	Sintered	Cold pressed and sintered	Flame melted	Sintered	Sintered reaction bonded
Additives	≤ 0.5 wt% MgO	4.9 wt% Y <sub>2</sub> O <sub>3</sub>	≤0.5 wt% MgO	None	6 wt% Y <sub>2</sub> O <sub>3</sub>	5 wt% Y <sub>2</sub> O <sub>3</sub> + 4 wt% MgO
Phase	$\alpha$	$\alpha$	$\alpha$	Amorphous	$\beta'$	$\beta$
Purity	≥99.5 wt%	94.0 wt%	99.5 wt%	99.995 wt%	94 wt%	91 wt%
Relative density	≥98%	≥99%	94.8%	100%	≥99%	≥99%
Nominal grain size	5 $\mu\text{m}$	7 $\mu\text{m}$ polyhedral	15 $\mu\text{m}$ equiaxed	Amorphous	2 $\mu\text{m}$	2 $\mu\text{m}$ equiaxed and 10 $\mu\text{m}$ acicular

Details regarding measurement techniques may be found in the original reports.

Several of the properties considered are intrinsic to the inter-atomic bonding in the material, namely density, elastic moduli, Poisson's ratio, specific heat capacity, and thermal expansion coefficient. Extrinsic "properties" are strongly dependent upon external factors such as processing, forming, finishing, and environmental conditions. Flexural, tensile and compressive strength, and thermal conductivity are considered extrinsic material properties because of their dependence on external factors. However, although the intrinsic material properties are directly related to inter-atomic bonding, the property exhibited by the bulk polycrystalline material is to a greater or lesser extent still affected by processing. For example, sintering temperature affects bulk density, which in turn affects the elastic moduli. Sintering conditions can also affect the amount of intergranular glass formed, thus affecting the thermal expansion coefficient. Intrinsic material properties are only independent of processing in single crystals.

### Ceramic materials for the GCT

Ceramic material properties are strongly dependent on raw powder, impurity, and sintering aid composition, and on forming and sintering parameters. For tractability, this study focuses on one particular material specification for each candidate material, based on one or more of: material purity, relative density, sintering aids, and mean grain size. The specification in each case is chosen to be representative of a high-performance commercially available material, in an attempt to bound the performance envelope of each material class. Material property data have been compiled from published original experimental studies, and from some first principle computational physics studies. Data compiled in some previous material property reviews are also considered. An excellent review of the mechanical and thermal properties of  $\alpha$ -alumina is provided by Munro [17] up to elevated temperatures. Alumina is considered in this review

for completeness: some data values from the Munro review [17] are given, along with data from more recent studies, and different studies of alumina not included in the Munro review. Where known, manufacturer-supplied data are not used. Every attempt has been made to find data corresponding to these specifications, and where data are unavailable, data for similar material specifications are used, and the differences in composition is noted. The material specifications used in this review are summarised in Table 2.

### Alumina

$\alpha$ -Alumina (Al<sub>2</sub>O<sub>3</sub>), the industry standard for electronic substrates [18], is widely used in high-heat flux electrical insulation, electronic packaging, and structural applications due to its relatively high strength, thermal conductivity, maximum service temperature, good chemical inertness, high electrical resistivity, low dielectric loss factor, and low-cost relative to other technical ceramics. Alumina is also widely used as a cutting tool, an RF window material, and is a candidate material for various applications in ITER [19–21]. ITER, a tokamak fusion plasma device, similarly requires electrically-insulating materials with high-thermal diffusivity and low dielectric loss tangent in many areas.

Alumina is available in a wide range of purities, with thermal and mechanical properties improving with increasing purity and relative density. 0.2 wt% MgO is commonly used as a sintering aid for Al<sub>2</sub>O<sub>3</sub> to prevent anomalous grain growth. The material specification used in this review for alumina is sintered  $\alpha$ -Al<sub>2</sub>O<sub>3</sub> with purity ≥99.5 wt%, relative density of ≥98% and a nominal grain size of 5  $\mu\text{m}$  [17], consistent with typical high performance, high-purity commercial grades of alumina.

### Aluminium Nitride

Aluminium nitride (AlN) has very high-RT thermal conductivity for a ceramic, second only to beryllia, with an

intrinsic thermal conductivity of  $319 \text{ W m}^{-1} \text{ K}^{-1}$  along the *c*-axis at 300 K [22], high-purity single-crystal RT thermal conductivity of  $285 \text{ W m}^{-1} \text{ K}^{-1}$  along the *c*-axis [22], and sintered body RT thermal conductivities over  $265 \text{ W m}^{-1} \text{ K}^{-1}$  reported [23, 24], although careful control of material composition and processing conditions is required to produce high-thermal conductivity bodies [25]. The thermal shock resistance of aluminium nitride is even higher than that of beryllia due to its lower coefficient of thermal expansion, closely matched to that of silicon. AlN is an attractive, non-toxic alternative to BeO for high-power electronic substrates, packages and heat spreaders, where thermal management is a significant design issue [26–34]. Other applications of AlN include its use for boats and crucibles for the production of high purity GaAs for semiconductor applications [35], and AlN has also been considered for use as a ballistic armour material [36]. However, use of AlN in structural applications has been limited, despite its good room temperature and elevated temperature mechanical properties. This is primarily due to high cost, typically making use of AlN only feasible where heat flux issues are severe. AlN has good oxidation resistance, due to the formation of a passivating alumina coating, even as high as  $1400 \text{ }^\circ\text{C}$  [37].

The thermal conductivity of AlN ceramics is greatly affected by the presence of metallic impurities [38], and oxygen impurity [39–41] present on the surface of the starting AlN powder in the form of  $\text{Al}_2\text{O}_3$  due to spontaneous reaction with air, and also dissolved in the AlN lattice. The lattice distortion due to aluminium vacancies resulting from incorporation of oxygen into the lattice leads to increased phonon scattering, thus lowering the thermal conductivity of the material [25, 42–46].

Rare-earth or alkaline-earth oxide additives are commonly used to facilitate liquid-phase sintering by reaction of the additive with  $\text{Al}_2\text{O}_3$  on the surface of the AlN powder, forming liquid phases [25] which promote densification. The additives are also used to react with oxygen impurity diffused from the AlN grains to the grain boundaries, forming secondary phase aluminates, thus reducing the number of oxygen defects and enhancing the thermal conductivity [25]. Yttria is the most commonly used sintering aid for AlN [47]. Achievement of maximum thermal conductivity requires optimization of the amount of additive, balancing between purification of AlN grains and formation of low thermal conductivity aluminate secondary phases [25].

Segregation of secondary phases from AlN grains occurs during annealing. Long annealing times or very high annealing temperatures facilitate the migration of aluminate secondary phases to the surface of the sintered body, with subsequent evaporation from the surface, improving the thermal conductivity [25]. However, annealing leads to

grain growth which, although contributing to enhancement of thermal conductivity, can reduce strength. AlN without additives typically requires hot pressing to achieve densification.

Fully dense AlN can be achieved by pressureless sintering with sintering aids. Structural AlN components are produced by either hot pressing or sintering. A typical high-performance commercially available grade of AlN is sintered, starting from a powder of 98.9 wt% Al + N and 1.1 wt% oxygen impurity content, to which 4.9 wt%  $\text{Y}_2\text{O}_3$ —an amount equimolar to the oxygen in the form of  $\text{Al}_2\text{O}_3$  present in the AlN powder—is added. A nominal grain size of  $7 \mu\text{m}$  and a relative density of  $\geq 99\%$  is specified.

### Beryllia

The room temperature thermal conductivity of beryllia (BeO) is the highest of any ceramic, close to that of high-conductivity metals, but decreases rapidly between room temperature and  $200 \text{ }^\circ\text{C}$ . Its high-thermal conductivity gives beryllia excellent thermal shock resistance, despite a high thermal expansion coefficient, and only moderate strength. BeO is extremely expensive, resulting from high powder cost and safety precautions required during powder handling and processing due to the fact that it is toxic. Despite its toxicity, the combination of excellent thermal and electrical properties, including low relative permittivity and dielectric loss tangent, makes beryllia a candidate material for a diverse range of high-technology applications. BeO is used in high-power and high-frequency electronic applications for substrates, heat sinks, and insulators where high-heat dissipation is required [18], in X-ray windows and high-power laser tubes, and in high-power RF-waveguide windows [48]. BeO is also considered for use in military applications for radomes and missile nosecones [49]; in aerospace applications for rocket motor nozzles; in materials processing applications as a refractory for molten metal handling and as a crucible and crucible-liner material; in nuclear applications for reactor moderator rods and neutron reflectors [50]; and as a potential material for vacuum windows of coaxial transmission lines in ITER [19, 51].

Typical impurities present in BeO powders include Fe, Mg, Ca, and Al [52, 53].  $\text{SO}_3$  and  $\text{SO}_4$  impurities may also be present in sulphate-derived powders, such as Brush-Wellman (now Materion Ceramics, 6100 South Tucson Blvd., Tucson, AZ 85706, U.S.A.) grade UOX, remaining after the production of the BeO powder by decomposition of beryllium sulfate salt [52, 53]. BeO typically also has a number of significant anionic impurities, including F, P, S, and Si, typically not stated by manufacturers in the total impurity content [54]. These anionic impurities contribute

to the reduction in strength of BeO at moderate and high temperatures requiring the use of high-purity powders, particularly powders low in F, P, S, and Si to retain good strength at these temperatures [54]. However, these anionic impurities also assist in the densification of BeO through reaction with a MgO sintering aid [54]. MgO, in the presence of impurities, has been found to be an effective sintering aid to promote densification of BeO [52, 54], typically added in quantities of  $\approx 0.5$  wt%. Iron is one of the most significant impurities in BeO, increasing the sinterability of BeO, allowing sintering to be achieved faster and/or at lower temperatures. However, Fe impurity leads to flaws and inhomogeneities in the sintered ceramic, and may also limit the achievable maximum sintered density [55]. Significant Fe pickup can occur from steel powder mixing equipment, particularly during long mixing times [53], and green body compaction equipment, which can lead to large irregular grains on the surface of the sintered ceramic [55]. Similarly, carbon pickup can occur from dies and pressing equipment, particularly affecting the surface layer of the BeO ceramic [56]; this necessitates the use of machining to remove this layer [54].

Cold uniaxial pressing [53], isostatic pressing and extrusion [55] are the most common techniques commercially used for forming green bodies from BeO powder [57], with large BeO bodies typically formed by isopressing [57]. Extrusion leads to some preferential grain orientation, the *c*-axis tending to align with the extrusion axis [58, 59], leading to some anisotropy in the sintered body [57]. BeO may be hot pressed [54], although this is less commercially prevalent than sintering. Hot pressing of BeO can achieve simultaneously higher density and finer grain size than sintering [54]. However, the shape of components that may be produced is typically somewhat limited to simple shapes; complex shapes require specially designed dies [54]. Hot pressing of BeO typically results in an anisotropic microstructure, with preferential alignment of the elongated *c*-axis of acicular grains in a plane perpendicular to the hot pressing direction with random orientation within this plane [60, 61].

The densification rate of BeO during sintering reduces above 94–95%td (6–5% porosity) due to isolation of grain boundary porosity, becoming very significant above  $2.90 \text{ g cm}^{-3}$  (96.4%td) [53, 55]. Subsequent reduction in porosity, via longer sintering times or higher temperatures, occurs slowly, and at the expense of increased grain growth [53, 55]. Peak strength in sintered BeO typically occurs in the density range  $2.81\text{--}2.93 \text{ g cm}^{-3}$ , due to the conflicting effects of densification and grain growth [53].

A typical high-performance grade of beryllia, is 99.5 wt% pure BeO. A typical commercially available grain size of  $15 \mu\text{m}$ , giving a good balance between strength and thermal conductivity, is specified here.

Typical relative density for sintered beryllia is  $\approx 94.8\%$  with very low-porosity bodies only being attainable at the expense of increased grain growth or use of hot pressing [54]. High purity starting powders are required, as anionic impurities, especially Si, F, P, and S lead to lower strength at moderate temperatures [54].

#### Fused quartz

The near-zero thermal expansion coefficient of fused quartz over a wide temperature range results in excellent thermal shock resistance. This property, combined with adequate strength, excellent corrosion resistance, ablation resistance, and excellent electrical properties, makes fused quartz the material of choice for a wide range of applications, including radomes, radar windows, combat, and space vehicles [62], vacuum windows [63, 64], boats and crucibles for high-temperature material handling and fabrication, and high-power lamp tubing. Owing to the high purity of fused quartz, its properties are very sensitive to small changes in composition and thermal history [65]. The hydroxyl content of fused quartz is one of the major impurities that affects its properties.

The typical high-performance commercially available grade of fused quartz specified here has less than 50 ppm total elemental impurities by weight, corresponding to a nominal purity of  $\geq 99.995$  wt%  $\text{SiO}_2$ . Flame melting of the quartz crystals is specified as the nominal processing route, but data for material produced by electrical melting of quartz crystals are considered where data are unavailable for material produced by a flame melting route. A fully dense amorphous material with no bubble inclusions is specified.

#### Sialon

Sialon (or ‘SiAlON’) is a solid solution based on silicon nitride, with  $\text{Al}^{3+}$  and  $\text{O}^{2-}$  replacing  $\text{Si}^{4+}$  and  $\text{N}^{3-}$  in the crystal lattice [66–70], resulting in a material with high strength, wear resistance, thermal shock resistance, and oxidation resistance [71]. The phases of sialon of interest for engineering applications are  $\alpha'$  [72, 73] ( $M_x\text{Si}_{12-(m+n)}\text{Al}_{m+n}\text{O}_n\text{N}_{16-m}$ , ( $x \leq 2$ ), where *M* is a metal cation), isostructural with  $\alpha$ - $\text{Si}_3\text{N}_4$ , and  $\beta'$  [66, 67] ( $\text{Si}_{6-z}\text{Al}_z\text{O}_z\text{N}_{8-z}$ , ( $0 \leq z \leq 4.2$ )), isostructural with  $\beta$ - $\text{Si}_3\text{N}_4$ , with duophase  $\alpha' + \beta'$  sialons also in common use.  $\beta'$ -sialon is the most widely used sialon, with higher fracture toughness ( $\approx 7\text{--}8 \text{ MPa m}^{\frac{1}{2}}$  for  $\beta'$ -sialon,  $\approx 3\text{--}4 \text{ MPa m}^{\frac{1}{2}}$  for  $\alpha'$ -sialon [74]) and room temperature strength, but lower hardness ( $\approx 1500\text{--}1700 \text{ kg mm}^{-2} \text{H}_v$  for  $\beta'$ -sialon,  $\approx 1900\text{--}2100 \text{ kg mm}^{-2} \text{H}_v$  for  $\alpha'$ -sialon) and thermal shock resistance than

$\alpha'$ -sialon [71, 75, 76]. A good combination of strength, hardness, and fracture toughness, intermediate to those of monolithic  $\alpha'$  and  $\beta'$ -sialons, can be obtained from duplex sialons [75], with hardness and thermal shock resistance increasing and toughness decreasing with increasing  $\alpha'$ -phase content [71, 77]. The higher lattice asymmetry and increased defects from greater Al–O and Si–N substitution, and the presence of interstitial cations, results in lower-thermal conductivity in  $\alpha'$ -sialon due to increased phonon scattering [78].

Oxynitride glasses occur as grain boundary phases (intergranular film at triple point junctions) in  $\text{Si}_3\text{N}_4$  and sialon ceramics, due to reaction of alumina and metal oxide sintering aids (such as yttria and other rare-earth oxides) with  $\text{SiO}_2$  on the surface of the  $\text{Si}_3\text{N}_4$  powder forming a liquid, which aids densification via liquid-phase sintering [79]. The thermo-mechanical properties of oxynitride glasses depend on various factors, including N:O ratio, modifier cations present and relative amounts of these modifier cations [79]. The properties of the oxynitride glass and the volume fraction present control the bulk properties of the sialon (or silicon nitride), having lower elastic moduli and higher thermal expansion coefficients than the sialon (or silicon nitride) grains [79]. The oxynitride glassy grain boundary phase typically present in  $\beta'$ -sialon ceramics leads to a deterioration in chemical and mechanical properties at elevated temperatures [71], reducing high-temperature strength and creep resistance due to glassy phase softening. This limits the practical maximum operating temperature to approximately 1,000 °C. Increasing the nitrogen content incorporated into the oxynitride glass results in higher glass transition temperature, viscosity, hardness, elastic moduli, and a decrease in the thermal expansion coefficient due to increased cross-linking in the glass due to the presence of N atoms [79].

For oxynitride glasses containing rare-earth cations, a decrease in the cation radius results in higher glass transition temperature, viscosity, and Young's modulus [79]. Lower viscosity oxynitride glass formed during sintering allows easier densification, but impairs creep resistance: metal cations such as Dy, Lu, Er, and Ho have smaller ionic radii than Y, and thus form higher viscosity oxynitride glasses with improved creep resistance [79].

The cations of metal oxide sintering aids used to stabilise the  $\alpha'$ -phase in the production of  $\alpha'$ -sialon may be interstitially incorporated into the solid solution, and this results in reduced volume of intergranular glassy phase [71].  $\alpha'$ -sialons consequentially retain their mechanical properties better at elevated temperatures and have a higher maximum operating temperature (up to 1,400 °C).

Sialons may be heat-treated, and this partially or fully crystallises the oxynitride grain boundary glass, forming a glass-ceramic or fully crystalline ceramic leading to

improvement in elevated temperature properties [79]. Complete devitrification is capable of raising the maximum operating temperature from  $\approx 1,000$  to  $\approx 1,400$  °C. The crystalline phases formed depend on the original glass composition and heat treatment parameters, and typically have considerably better mechanical properties than the parent glass (e.g.,  $E > 200$  GPa) [79].

$\beta'$ -sialon typically has acicular grains [71, 80], while  $\alpha'$ -sialon typically has equiaxed grain structure [71], but can be produced with a bimodal equiaxed-acicular microstructure by careful selection of starting composition and control of sintering conditions, or use of elongated seed crystals in the starting powder [81], with resultant improved fracture toughness and thermal shock resistance [82]. The intrinsically higher fracture toughness of  $\beta'$ -sialon is due to the in situ reinforced microstructure. The equiaxed microstructure typically found in single-phase  $\alpha'$ -sialon leads to lower room temperature flexural strength, typically in the range 350–500 MPa (compared to  $\approx 700$ –1100 MPa for  $\beta'$ -sialon), with higher reported values for single-phase  $\alpha'$ -sialons with acicular grains or duophase sialons with high  $\alpha'$ -phase content.

$\alpha'$ -phase sialon can transform to  $\beta'$ -phase at high temperature in the presence of liquid-phase oxynitride glass [71, 79]. The stability of the  $\alpha'$ -phase is dependent upon the metal cations present in the sintering aid, and the ability to stabilise the  $\alpha'$ -phase is a major consideration in the selection of a sintering aid for  $\alpha'$ -sialon. Sintering aids used for  $\alpha'$ -sialon are typically Y [76], Ca, Mg, Li, or rare-earth metals (such as Nd, Sm [75], Dy, Yb [83]) except La and Ce [71], with dysprosium (Dy) found to be very effective at stabilizing the  $\alpha'$ -phase [75, 84]. There have been a number of studies on suppressing  $\alpha'$ – $\beta'$  phase transformation, with subsequent improvement in material properties.

The most common formation route for  $\alpha'$ -sialon is by direct sintering of  $\alpha$ - $\text{Si}_3\text{N}_4$ , AlN,  $\text{Al}_2\text{O}_3$ , and other metal oxide powders [71]. Liquid-phase sintering is achieved by reaction of  $\text{Al}_2\text{O}_3$  and metal oxide sintering aids with  $\text{SiO}_2$  on the surface of the  $\text{Si}_3\text{N}_4$  powder, forming a liquid phase which aids densification [79]. Sialon may also be fabricated by nitridation of powders and post-sintering [71], typically with higher resultant porosity and inferior mechanical properties than direct sintering. A large number of studies have been conducted on the preparation of sialon ceramics over the past four decades [85], with significant improvement in sialon properties achieved. The retention of many desirable properties at elevated temperatures, including strength, wear resistance, hardness, corrosion and oxidation resistance, creep resistance, good thermal shock resistance, and low coefficient of thermal expansion, makes sialons promising materials for a wide range of high temperature, high-stress applications in corrosive environments. Applications of sialons include cutting tools, dies, diesel fuel valves, and weld locator pins [86]. Sialons are also

considered as candidate materials for, amongst other applications, radomes [87], and gun barrel liners [83].

$\alpha'$ -sialons have many superior properties to  $\beta'$ -sialons salient to the application being addressed here, including higher thermal shock resistance and higher maximum service temperature, despite their lower thermal conductivity and strength at room temperature and intermediate temperatures. However, research into  $\alpha'$ -sialons is still less mature than for  $\beta'$ -sialons, and the vast majority of commercially available sialons are  $\beta'$ -phase or duophase. In addition, the data on the mechanical properties of  $\alpha'$ -sialons are widely scattered, partly due to microstructural and compositional variation [71]. Therefore, for this review,  $\beta'$ -sialon is selected as the nominal phase, but data for duophase sialons are also considered. Y- $\beta'$ -sialon with 6 wt%  $Y_2O_3$  sintering aid is chosen as the material specification for this study, with relative density of  $\geq 99.0\%$ , nominal grain size of 2  $\mu\text{m}$ , and nominal purity of 94 wt%  $Si_3N_4 + AlN + Al_2O_3$ . Given the volume of ongoing research into  $\alpha'$ -sialons, and their attractive intrinsic properties, it is conceivable that  $\alpha'$ -sialons will surpass  $\beta'$ -sialons as a candidate material for this application in the coming years.

### Silicon nitride

Silicon nitride ( $Si_3N_4$ ) is one of the most attractive materials for high-temperature structural and electronic applications, due to its hot strength, toughness, thermal shock resistance, thermal conductivity, and dielectric properties. It has two polymorphic forms of interest;  $\alpha$  and  $\beta$  [88, 89].  $\alpha$ -phase  $Si_3N_4$ —a metastable phase under ordinary pressures [90] with lower thermal conductivity—transforms to  $\beta$ - $Si_3N_4$  at high temperature, making  $\beta$ - $Si_3N_4$  more suitable for engineering applications [91]. Silicon nitride for structural applications may be produced near theoretical density by a variety of processing methods, including hot pressing (HPSN), hot isostatic pressing (HIPS), pressureless sintering (SSN), gas-pressure sintering (GPSN), and sinter-reaction bonding (SRBSN), with material properties dependent upon processing route. The 15–30% porosity typical in reaction-bonded silicon nitride (RBSN) results in comparatively inferior mechanical ( $\sigma_f \approx 200$  MPa [92],  $E \approx 130$ – $200$  GPa) and thermal properties [93], making it less suitable for structural applications. SRBSN is produced by nitriding a mixture of silicon powder and sintering aids, green-machining, and then sintering to densify the component. An advantage of the SRB process is that it allows near-net shape fabrication of complex  $Si_3N_4$  components, whereas HP and HIP processes only allow for the production of simply shaped components, with any post-sinter grinding adding significantly to component cost. HIP results in the highest strength silicon nitrides, comparable to that of HPSN (800–1200 MPa), with that of SSN slightly lower

(600–1000 MPa) [92]. SRBSN has shown the greatest potential for having simultaneously high-thermal conductivity and strength [94]. The toughening effect of silicon nitride's bimodal microstructure, due to crack bridging, is controlled by the size and volume fraction of the large acicular grains [81]. Extensive research over the past four decades has significantly improved the thermal [91], creep [95, 96], and mechanical properties of silicon nitrides [81], notably simultaneously improving strength, fracture toughness [81], and thermal conductivity [94]. Strong, high thermal conductivity  $Si_3N_4$  ceramics may be attainable with use of high-purity sub-micron powders, and careful selection of sintering aids.

Owing to the low diffusion coefficient of silicon nitride [71], densification requires the use of sintering aids to facilitate liquid-phase sintering by formation of an oxynitride glass [79]. Pressureless sintering of silicon nitride requires large additions of sintering aids to achieve full densification [76]. Some of the oxynitride glassy phase always remains, impacting on the material's mechanical properties, particularly at high temperatures [71], limiting the maximum operating temperature to  $\approx 1000$ – $1200$  °C [92]. Fully dense HPSN and HPSN can be produced with very small additions of sintering aids, yielding reduced glassy phase. This results in excellent mechanical properties which are retained to higher temperatures, with maximum operating temperatures of  $\approx 1200$ – $1300$  °C [76, 92]. Typical sintering aids used for the densification of silicon nitride are yttria ( $Y_2O_3$ ), alumina ( $Al_2O_3$ ), magnesia ( $MgO$ ), and rare-earth oxides, either singly or in combination [71, 91], with calcium oxide ( $CaO$ ) and various other compounds also successfully used.  $Al_2O_3$  is an inexpensive sintering aid, but unlike  $Y_2O_3$  and  $MgO$  it forms a solid solution in the  $Si_3N_4$  grains, leading to significantly lower thermal conductivity. Use of  $MgO$  and  $Y_2O_3$  sintering aids in combination yields low porosity, high strength silicon nitride [97].

The combination of thermal, dielectric, wear, and superior high-temperature mechanical properties has led to implementation of silicon nitride in a wide range of ambient and high-temperature structural and electronic applications, including cutting tools, turbocharger rotors, reciprocating engine valves, bearings, rocket motor components, electronic substrates and heat sinks, RF waveguides, windows, and radomes. Silicon nitride has been long proposed for use in the hot section of gas turbines, as rotors, stators and combustion liners, but deployment has been limited due to low fracture toughness, which limits impact resistance, and oxidation and environmental degradation in the high-temperature, high-velocity combustion environment which leads to removal of the  $SiO_2$  protective layer [81].

SRBSN is selected as the nominal production route for  $Si_3N_4$  for the current work, due to its potential for having simultaneously high thermal conductivity and strength

[94]. Data are also considered for SSN, HIPSN, and HPSN materials representative of commercially available silicon nitrides. A typical high-performance commercially available grade of silicon nitride is sinter-reaction bonded  $\beta$ - $\text{Si}_3\text{N}_4$  produced with 5 wt% MgO, 4 wt%  $\text{Y}_2\text{O}_3$  sintering aids, corresponding to 91 wt% purity of silicon nitride powder mix. The expected microstructure is bimodal with fine  $\approx 2 \mu\text{m}$  equiaxed grains and larger acicular grains with average major axis length  $\approx 10 \mu\text{m}$ . A relative density of  $\geq 99\%$  are specified.

## Structural material properties

### Density

The practical bulk density of the six materials in this study, as supplied commercially, is sought. Density is dependent upon the amounts and types of sintering aids used; such as the high-molecular mass sintering aids commonly used with AlN, sialon, and  $\text{Si}_3\text{N}_4$  such as  $\text{Y}_2\text{O}_3$ ; upon the presence of other impurities, and upon the resulting secondary phases formed [76].

The theoretical density of pure ceramic crystals may be calculated from measurements of the lattice parameters. For hexagonal lattices the unit cell has volume  $V = (\sqrt{3}/2)a^2c$ , where  $a$  and  $c$  are the respective lattice parameters. The theoretical density can be calculated from:

$$\rho_{\text{th}} = \frac{Mz}{N_A V} \quad (1)$$

where  $z$  is the number of formula units per unit cell,  $N_A$  is Avogadro's number, and  $V$  is the unit cell volume, and  $M$  is the molar mass. The theoretical density may be used as an estimate of the bulk density of very low-porosity polycrystalline ceramics in the absence of significant secondary phases or intra-granular solid solution formation. For sintered AlN, sialon, and  $\text{Si}_3\text{N}_4$  the large mass fraction of sintering aids typically used precludes the use of this calculation method for accurate estimation of sintered ceramic density. Direct experimental measurements of ceramic density at high temperature are typically not found in the literature, but elevated temperature measurements of lattice parameters from X-ray diffraction and linear thermal expansion from dilatometry may be used to assess variations in density with temperature.

Taylor and Lenie [37] calculated the theoretical density of AlN to be  $\approx 3.26 \text{ g cm}^{-3}$  from lattice parameter measurements of single crystals. Hot pressing of AlN to very low levels of porosity with little or no sintering aid addition results in a practical bulk density very close to this theoretical value (e.g., as measured in [98]). However, low-

porosity sintered or hot pressed AlN with additions of high-molecular mass sintering aids such as  $\text{Y}_2\text{O}_3$  have bulk densities higher than this, with bulk density typically increasing with increasing sintering aid addition [28]. By analysing the data, the density of fully dense AlN may be approximated by:

$$\rho_{\text{Y-AlN}} \cong 3.26 + 13 \times 10^{-3} \xi_{\text{Y}_2\text{O}_3} \quad (2)$$

where  $\xi_{\text{Y}_2\text{O}_3}$  is the yttria addition in wt%.

Commercial BeO is typically produced with density  $\approx 2.85 \text{ g cm}^{-3}$ , having  $\rho_{\text{th}} \approx 94.7\%$ , or to a lesser extent with density  $\approx 2.90 \text{ g cm}^{-3}$  and  $\rho_{\text{th}} \approx 96.3\%$ . Beryllia may be produced near full density, but typically at the expense of increased grain growth, with corresponding deterioration in mechanical properties. A theoretical density of  $3.008 \text{ g cm}^{-3}$  was calculated for BeO by Lillie [58] from lattice parameter measurements, and is used by several authors (e.g., by Beaver et al. [52]). However, a more extensive analysis of lattice parameter values from the literature indicates that the true theoretical density is  $\approx 3.0104 \text{ g cm}^{-3}$ , with a value of  $3.010 \text{ g cm}^{-3}$  being widely used in the literature (e.g., in [54]).

The density of fused quartz is significantly lower than that of the ceramics considered in this study. Sosman [99] notes relatively large variations in literature values of density of vitreous silica, both within specimens and between different specimens, on the order of 0.1%—much more scatter than for literature values of crystalline quartz—possibly due to composition, type of silica from which the vitreous silica was made, temperature history during manufacture, strain fields in the glass, or small amounts of impurities.

The density of the  $\alpha'$ -,  $\beta'$ -sialon, and oxynitride glassy phases are approximately 3.28, 3.18, and  $4.00 \text{ g cm}^{-3}$ , respectively, [76]. The density of the  $\beta$ - $\text{Si}_3\text{N}_4$  phase is approximately  $3.2 \text{ g cm}^{-3}$ . The lattice volume of  $\alpha$ - $\text{Si}_3\text{N}_4$  is 0.55% larger than that of  $\beta$ - $\text{Si}_3\text{N}_4$  per  $\text{Si}_3\text{N}_4$  unit [90].

Experimental measurements of density are plotted in Fig. 1.

### Young's, bulk, and shear moduli

The elastic moduli, including the Young's, shear, and bulk moduli, and the Poisson's ratio, of isotropic solid materials may be calculated from measurements of the density and longitudinal and shear sound velocities by ultrasonic methods [17, 102, 111]:

$$E = \rho \left( \frac{3V_L^2 V_S^2 - 4V_S^4}{V_L^2 - V_S^2} \right) \quad (3)$$

$$G = \rho V_S^2 \quad (4)$$

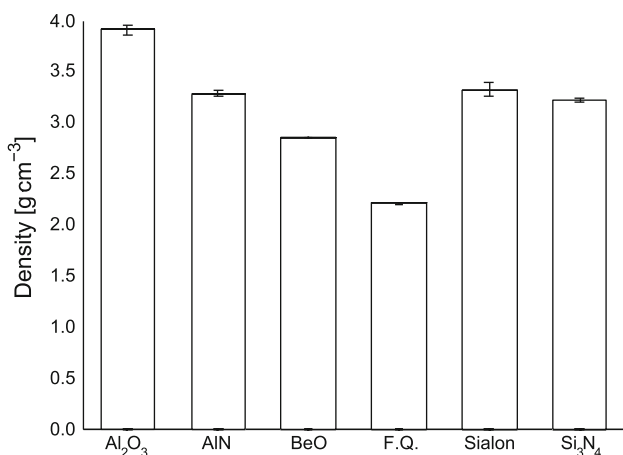


**Fig. 1** RT Density values averaged from the following references: Al<sub>2</sub>O<sub>3</sub>-1, CoorsTek AD995 alumina [100]; Al<sub>2</sub>O<sub>3</sub>-2, Coors AD-998 alumina [101]; Al<sub>2</sub>O<sub>3</sub>-3, Wesgo AL-998 Alumina [101]; Al<sub>2</sub>O<sub>3</sub>-4, review of alumina [17]; AlN-1, Cercom hot pressed AlN [98]; AlN-2, HP AlN with ≈4 wt% Y<sub>2</sub>O<sub>3</sub> [102]; AlN-3, sintered AlN with 0.5 mol% Y<sub>2</sub>O<sub>3</sub> [103]; AlN-4, sintered AlN 5 wt% Y<sub>2</sub>O<sub>3</sub> [28]; AlN-5, sintered AlN 4.91 wt% Y<sub>2</sub>O<sub>3</sub> [25]; AlN-6, Cerac HP AlN [104]; AlN-7, HP AlN [105]; BeO-1, Brush-Wellman 995 BeO [101]; F.Q.-1, review of fused quartz [99]; F.Q.-2, Toshiba Ceramics T-1030 fused quartz [106]; F.Q.-3, PECVD fused quartz film [107]; F.Q.-4, KU1 fused quartz [108]; F.Q.-5, Heraeus Infracril 301 fused quartz [108]; Sialon-1, Kennametal TK4 sialon [100]; Sialon-2, sintered sialon 6 wt% Y<sub>2</sub>O<sub>3</sub> [76]; Sialon-3, Kennametal TK4 sialon [83]; Si<sub>3</sub>N<sub>4</sub>-1, Ceradyne Ceralloy 147-31N silicon nitride [100]; Si<sub>3</sub>N<sub>4</sub>-2, Kyocera SN235P silicon nitride [100]; Si<sub>3</sub>N<sub>4</sub>-3, SR3 silicon nitride [94]; Si<sub>3</sub>N<sub>4</sub>-4, SR6 silicon nitride [94]; Si<sub>3</sub>N<sub>4</sub>-5, sintered Si<sub>3</sub>N<sub>4</sub> with 1 mol% Y<sub>2</sub>O<sub>3</sub>, and 1 mol% Nd<sub>2</sub>O<sub>3</sub> [109]; Si<sub>3</sub>N<sub>4</sub>-6, sintered Si<sub>3</sub>N<sub>4</sub> with 2 mol% Al<sub>2</sub>O<sub>3</sub>, and 2 mol% Y<sub>2</sub>O<sub>3</sub> [109]; Si<sub>3</sub>N<sub>4</sub>-7, HP Si<sub>3</sub>N<sub>4</sub> with 3.5 wt% Y<sub>2</sub>O<sub>3</sub> [110]; Si<sub>3</sub>N<sub>4</sub>-8, HP and HIP Si<sub>3</sub>N<sub>4</sub> with 3.5 wt% Y<sub>2</sub>O<sub>3</sub> [110]

$$K = \rho \left( V_L^2 - \frac{4}{3} V_S^2 \right) \tag{5}$$

$$\nu = \frac{V_L^2 - 2V_S^2}{2(V_L^2 - V_S^2)} \tag{6}$$

where *E*, *G*, and *K* are the Young’s, shear, and bulk moduli respectively, *ν* is the Poisson’s ratio, *V<sub>L</sub>* and *V<sub>S</sub>* are the longitudinal and shear sound velocities, respectively, and *ρ* is the density. In addition to ultrasonic methods, elastic moduli may be determined by a variety of experimental methods, including calculation of *E* from flexural tests and calculation of *K* from isostatic compressive tests. The first-order elastic response of isotropic solid materials is fully constrained by any two such moduli. The remaining two constants may be calculated by the standard relations:

$$E = 2G(1 + \nu) \tag{7}$$

$$K = \frac{E}{3(1 - 2\nu)} \tag{8}$$

$$\nu = \frac{3K - E}{6K} \tag{9}$$

$$G = \frac{3KE}{9K - E} \tag{10}$$

To ensure consistency between recommended values, curve fit equations for all elastic properties are solved simultaneously, constrained by these relations. A further consistency measure is to recognize that the Poisson’s ratio must always be in the range 0 < *ν* < 0.5 [112], and will be ≈0.2–0.3 for almost all of the materials under investigation, while for fused quartz *ν* ≈ 0.17. Differences between measurement of adiabatic and isothermal elastic values are ignored, the adiabatic moduli being assumed. Above 1000 °C, plasticity effects greatly influence the apparent elastic moduli calculated from static measurements such as flexural tests, so dynamic methods are preferred [58].

The Young’s, shear, and bulk moduli are strongly dependent upon the porosity of a ceramic, decreasing sharply initially, and then more gradually with increasing porosity. The porosity dependence of elastic moduli can be estimated by a simple linear model at very low porosities, while over a broad range of porosities the relationship is non-linear. A great number of models have been proposed to describe the variation in elastic moduli with porosity [113–116], notably including those of Hasselman [117], and Knudsen [118]. However, variation of elastic moduli is dependent not only on the volume of porosity but also its morphology, precluding use of one model to describe the variation for all materials [119].

The elastic properties of most non-cubic ceramic crystals are anisotropic, but polycrystalline ceramics composed of randomly oriented grains typically exhibit approximate macroscopically isotropic behavior [17]. However, processing routes which lead to preferential grain orientations, such as hot pressing, can result in macroscopic anisotropic behavior [104, 120]. De With and Hattu [104] measured differences in the Young’s modulus of hot pressed AlN without sintering aids in directions parallel and perpendicular to the hot pressing direction, while Fryxell and Chandler [59] observed anisotropic elastic moduli in BeO with preferential grain orientation, extruded and sintered from BeO powder containing needle-like crystals.

Crystals of the hexagonal crystal system have only five independent elastic constants: *C<sub>11</sub>*, *C<sub>12</sub>*, *C<sub>13</sub>*, *C<sub>33</sub>*, and *C<sub>44</sub>* [121], the elastic constant *C<sub>66</sub>* being given by *C<sub>66</sub>* = ½(*C<sub>11</sub>* – *C<sub>12</sub>*). Consistency criteria apply, limiting the valid range of elastic constant values, based on lattice stability [122, 123]. The compliance matrix may be evaluated from single-crystal ultrasonic wave velocity measurements or by other means. The macroscopically pseudo-isotropic

elastic moduli of a fully-dense ceramic composed of randomly oriented crystals may be estimated from the single-crystal elastic moduli using the Voigt-Reuss-Hill (VRH) approximation [124–126]. The isotropic VRH estimation of the bulk modulus is:

$$K_{\text{VRH}} = \frac{C_{11} + 2C_{12}}{3} \quad (11)$$

while the VRH estimation of the shear modulus is the average of the Voigt and Reuss limits on shear modulus:

$$G_{\text{VRH}} = \frac{G_{\text{V}} + G_{\text{R}}}{2} \quad (12)$$

$$G_{\text{V}} = \frac{(C_{11} - C_{12}) + 3C_{44}}{5} \quad (13)$$

$$G_{\text{R}} = \frac{5C_{44}(C_{11} - C_{12})}{(4C_{44} + 3(C_{11} - C_{12}))} \quad (14)$$

where  $C_{ij}$  are the relevant coefficients of the compliance matrix, and  $G_{\text{V}}$  and  $G_{\text{R}}$  are the Voigt and Reuss limits on shear modulus respectively. From these relations the VRH approximation of the Young's modulus and Poisson's ratio may be calculated using the standard relations for isotropic solid materials. Chung and Buessem [127] assert that the VRH method provides a good approximation to the polycrystalline elastic moduli for materials with single-crystal elastic anisotropy of <10%, defined by:

$$A^* = \left( \frac{3(A - 1)^2}{3(A - 1)^2 + 25A} \right) \times 100 \quad (\%) \quad (15)$$

where

$$A = \frac{2C_{44}}{C_{11} - C_{12}} \quad (16)$$

Reviews of elastic moduli of ceramics inevitably must consider data from materials of slightly different porosity levels. Correlation of data of different porosities, including calculations of moduli for the theoretically dense material using the VRH approximation, into porosity models allows for the estimation of the moduli at the nominally specified porosity level.

The presence of secondary phases affects the elastic moduli of ceramics (porosity being a limiting case of a secondary phase of zero stiffness). Glassy grain boundary phases are present in many ceramics, as discussed in [Sialon](#) and [Silicon nitride](#) sections, of varying volume fraction and morphology, leading to large differences in measured moduli values for ostensibly similar compositions. Oxynitride glassy phases found in sialons and silicon nitrides have lower elastic moduli ( $\approx 120$ – $170$  GPa) than the primary phase, reducing the Young's, shear, and bulk moduli of the bulk material [79].

The derivative with respect to temperature of any elastic constant tends toward zero approaching absolute zero

[128], while a linear dependence of Young's modulus with respect to temperature has been observed for many crystalline solids at high temperatures [128]. A simple linear fit has been used by several researchers for the temperature dependence of elastic moduli, as the deviation from linear variation with temperature is small except at low temperatures [129]. However, this fit can lead to a slight overestimation of the room temperature Young's modulus from intermediate or high-temperature data. The Wachtman equation has been shown to accurately describe the temperature dependence of Young's modulus—provided the variation in Poisson's ratio with temperature is small—or bulk modulus, across a broad range of temperature for various non-metallic crystals and polycrystalline ceramics [128, 130]:

$$Y = Y_0 - B \cdot T \cdot \exp\left(\frac{-T_0}{T}\right) \quad (17)$$

where  $Y_0$  is the Young's or bulk modulus at 0 K, and both  $T_0$  (K) and  $B$  (GPa K<sup>-1</sup>) are empirical fitting parameters, related to the Debye temperature and Grüneisen parameter. The slope of the Wachtman equation tends to  $-B$  at high temperature. The parameter  $T_0$  is relatively sensitive to small variations or errors in Young's or bulk moduli data [102]. Some deviation from linear behavior of Young's modulus of alumina has been observed by Wachtman and Lam [131] and Fukuhara and Yamauchi [132] at very high temperatures, and this is attributed to grain boundary slip [131]. Wolfenden [133] and Sánchez-González et al. [134] observed that the rate of decrease of Young's modulus with temperature of two commercially supplied aluminas increases rapidly above 600–800 °C, possibly due to grain boundary sliding arising from softening of a glassy secondary phase [134]. The rate of decrease of Young's modulus with temperature in the studies of Wolfenden and Sánchez-González et al. is significantly greater than that seen in many other studies of alumina, possibly due to larger volume fraction of glassy grain boundary phase, or occurrence of a brittle-to-ductile transition.

In contrast to polycrystalline ceramics, the elastic moduli of fused quartz increase with increasing temperature.

Data for Young's, bulk, and shear moduli of all materials are plotted in Figs. 2, 3, and 4, respectively.

#### Poisson's ratio

The Poisson's ratio,  $\nu$ , of polycrystalline ceramics is relatively insensitive to temperature compared to other elastic parameters, being widely taken as a constant, although some variation with temperature does occur [132]; typically it increases with temperature for the materials considered in this review. Poisson's ratio can be calculated

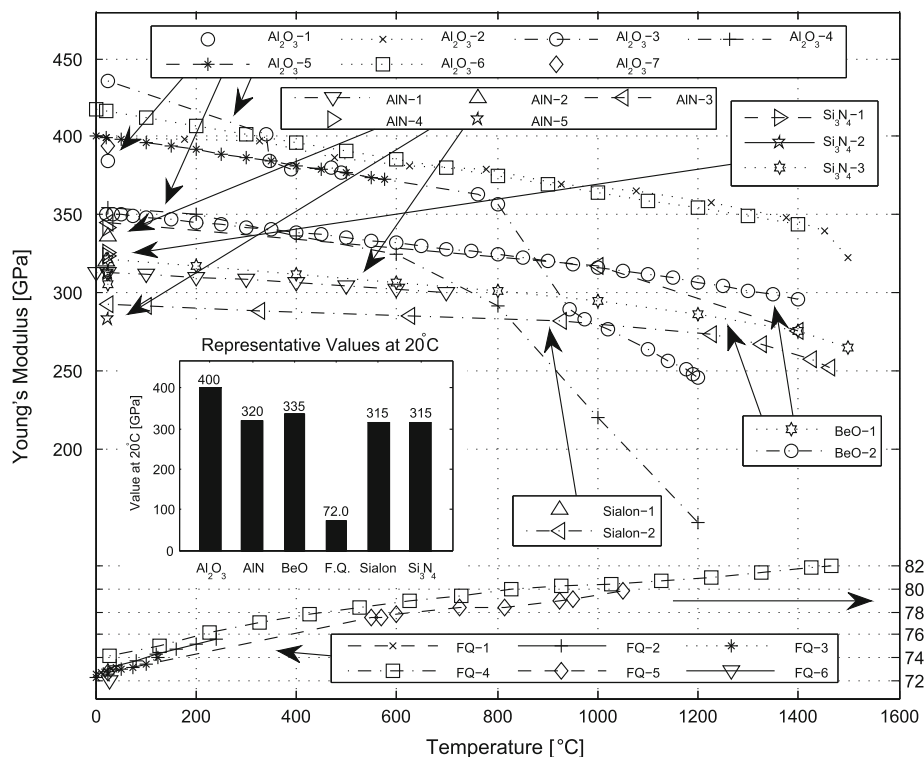


**Fig. 2** Young’s modulus values from the following references: Al<sub>2</sub>O<sub>3</sub>-1, CoorsTek AD995 alumina [100]; Al<sub>2</sub>O<sub>3</sub>-2, near-theoretical density alumina [132]; Al<sub>2</sub>O<sub>3</sub>-3, McDanel Refractory Company 99.8% pure alumina [133]; Al<sub>2</sub>O<sub>3</sub>-4, Goodfellow 98% dense alumina [134]; Al<sub>2</sub>O<sub>3</sub>-5, sintered alumina [128]; Al<sub>2</sub>O<sub>3</sub>-6, review of alumina [17]; Al<sub>2</sub>O<sub>3</sub>-7, hot pressed and HIPped alumina [135]; AlN-1, HP AlN with ≈4 wt% Y<sub>2</sub>O<sub>3</sub> [102]; AlN-2, Cercom HP AlN [98]; AlN-3, HP AlN [37]; AlN-4, Cerac HP AlN [104]; AlN-5, Keramont Corporation sintered AlN [136]; BeO-1, beryllia [58]; BeO-2, 94.8%t.d. BeO [59];

F.Q.-1, clear fused silica [137]; F.Q.-2, optical quality fused silica [138]; F.Q.-3, Toshiba Ceramics T-1030 fused quartz [106]; F.Q.-4, Toshiba Ceramics T-1030 fused quartz [139]; F.Q.-5, fused silica [140]; F.Q.-6, PECVD fused quartz film [107]; Sialon-1, Kennametal TK4 sialon [100]; Sialon-2, near-theoretical density β-sialon [132]; Si<sub>3</sub>N<sub>4</sub>-1, Ceradyne Ceralloy 147-31N silicon nitride [100]; Si<sub>3</sub>N<sub>4</sub>-2, Kyocera SN235P silicon nitride [100]; Si<sub>3</sub>N<sub>4</sub>-3, GTE Laboratories PY6 HIP silicon nitride [141]

from ultrasonic measurements or static (e.g., flexural) measurements. At high homologous temperatures the effects of creep become increasingly more pronounced causing static measurements of Poisson’s ratio to approach a limiting value of 0.5 [58], and this makes dynamic measurement more suitable. Poisson’s ratio may also be calculated from the Young’s and shear moduli:

$$\nu = \left( \frac{E}{2G} - 1 \right) \tag{18}$$

This relation holds only for isotropic materials, but may be applied to polycrystalline materials composed of randomly oriented anisotropic grains [147]. However, large variations are present in Poisson’s ratio measurements reported in the literature for the ceramic materials considered in this study. This may partly result from calculating the Poisson’s ratio from Young’s and shear moduli, which are calculated in turn from sound velocities or resonance frequencies, with small errors in Young’s and shear moduli leading to large errors in Poisson’s ratio.

Experimental data are plotted in Fig. 5.

### Flexural strength

There is a very wide variation in values reported for flexural strength of materials in the literature, due in part to differences in testing environment and surface finish [150]. In addition, flexural strength measurements must be treated cautiously, as the measured value depends upon the test configuration (3 or 4-point bend) and sample dimensions. For a given specimen size, the stressed volume in a three-point bend test is smaller, resulting in higher measured values of strength. The measured strength of ceramics is also dependent upon the strain rate of the measurement. Data presented here are for strain rates typical of quasi-static flexural, tensile, or compressive tests (loading rate ≈0.5 mm min<sup>-1</sup>), intermediate to those of shock testing and creep testing. At high-homologous temperatures, creep in ceramics becomes a significant design issue, requiring

**Fig. 3** Bulk modulus values from the following references:  $\text{Al}_2\text{O}_3$ -1, near-theoretical density alumina [132];  $\text{Al}_2\text{O}_3$ -2, review of alumina [17];  $\text{Al}_2\text{O}_3$ -3, hot pressed and HIPped alumina [135];  $\text{AlN}$ -1, Cercom HP  $\text{AlN}$  [98];  $\text{AlN}$ -2, 99.99% pure  $\text{AlN}$  [142];  $\text{AlN}$ -3, Tokuyama Soda and Toshiba Ceramics  $\text{AlN}$  [143];  $\text{AlN}$ -4, theoretical calculation for  $\text{AlN}$  [144];  $\text{BeO}$ -1, single-crystal  $\text{BeO}$  [145];  $\text{BeO}$ -2, 99.88%t.d. polycrystalline  $\text{BeO}$  [146]; F.Q.-1, Toshiba Ceramics T-1030 fused quartz [106]; Sialon-1, near-theoretical density  $\beta$ -sialon [132];  $\text{Si}_3\text{N}_4$ -1, theoretical calculation for  $\beta$ - $\text{Si}_3\text{N}_4$  [90]

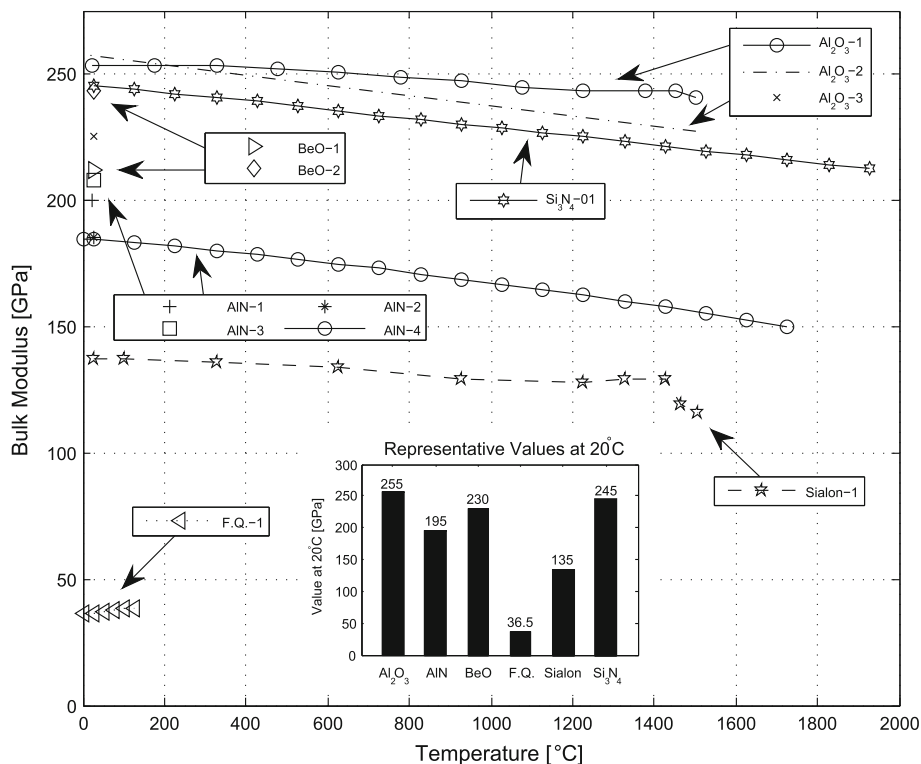
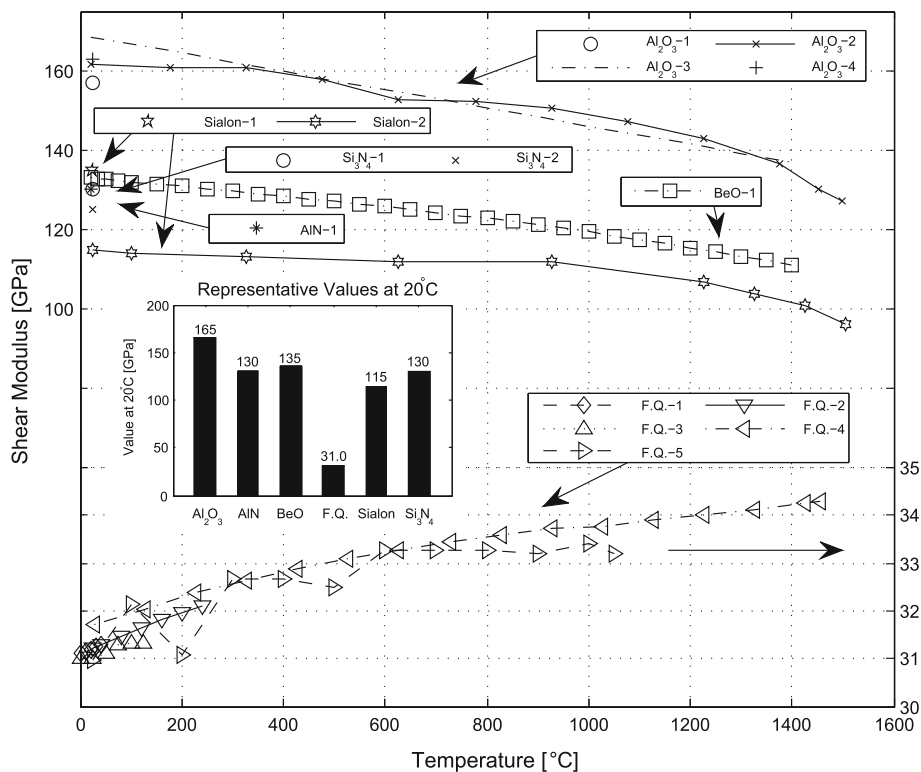


**Fig. 4** Shear modulus values from the following references:  $\text{Al}_2\text{O}_3$ -1, CoorsTek AD995 alumina [100];  $\text{Al}_2\text{O}_3$ -2, near-theoretical density alumina [132];  $\text{Al}_2\text{O}_3$ -3, review of alumina [17];  $\text{Al}_2\text{O}_3$ -4, hot pressed and HIPped alumina [135];  $\text{AlN}$ -1, Cercom HP  $\text{AlN}$  [98];  $\text{BeO}$ -1, 94.8%t.d.  $\text{BeO}$  [59]; F.Q.-1, clear fused silica [137]; F.Q.-2, optical quality fused silica [138]; F.Q.-3, Toshiba Ceramics T-1030 fused quartz [106]; F.Q.-4, Toshiba Ceramics T-1030 fused quartz [139]; F.Q.-5, fused silica [140]; Sialon-1, Kennametal TK4 sialon [100]; Sialon-2, near-theoretical density  $\beta$ -sialon [132];  $\text{Si}_3\text{N}_4$ -1, Ceradyne Ceralloy 147-31N silicon nitride [100];  $\text{Si}_3\text{N}_4$ -2, Kyocera SN235P silicon nitride [100]

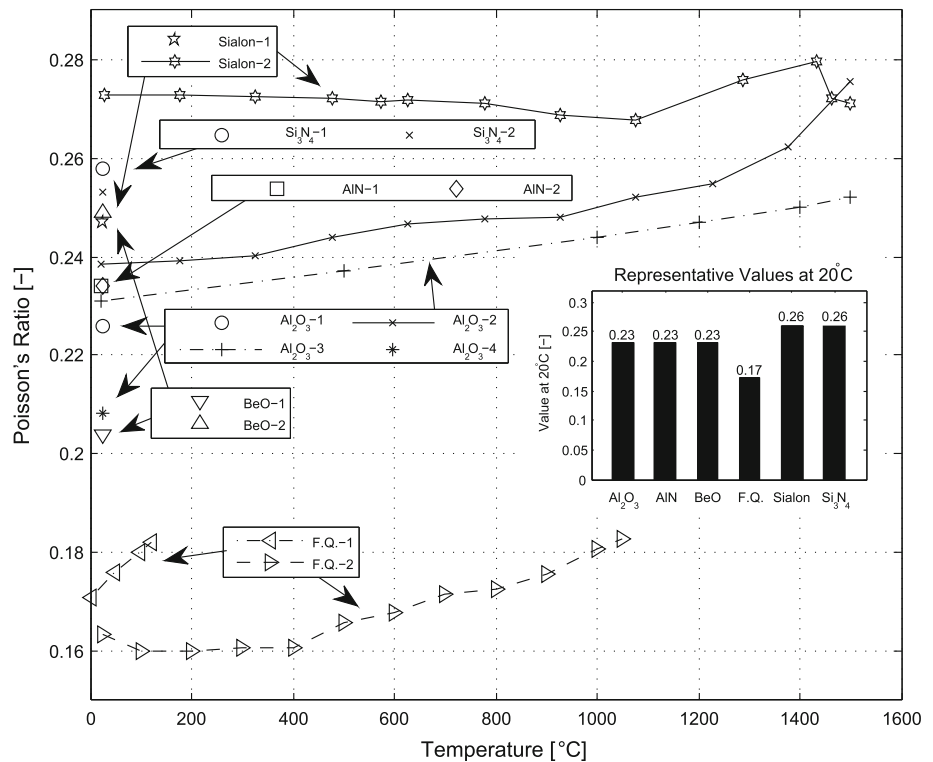


careful creep analysis, but collation of creep data is beyond the scope of this article.

Sintered or hot pressed alumina is commercially available in a wide range of purities, with strength increasing

with increasing purity. Some very high flexural, tensile, and compressive strength values have been reported in the literature for carefully prepared aluminas, produced from high-purity powders, with low porosity, small grain size,

**Fig. 5** Poisson's ratio values from the following references: Al<sub>2</sub>O<sub>3</sub>-1 CoorsTek AD995 alumina [100]; Al<sub>2</sub>O<sub>3</sub>-2, near-theoretical density alumina [132]; Al<sub>2</sub>O<sub>3</sub>-3, review of alumina [17]; Al<sub>2</sub>O<sub>3</sub>-4, hot pressed and HIPped alumina [135]; AlN-1, Cercom HP AlN [98]; AlN-2, Dow Chemical Corporation HP AlN [148]; BeO-1, fully dense BeO [58]; BeO-2, single-crystal BeO [149]; F.Q.-1, Toshiba Ceramics T-1030 fused quartz [106]; F.Q.-2, fused silica [140]; Sialon-1, Kennametal TK4 sialon [100]; Sialon-2, near-theoretical density β-sialon [132]; Si<sub>3</sub>N<sub>4</sub>-1, Ceradyne Ceralloy 147-31N silicon nitride [100]; Si<sub>3</sub>N<sub>4</sub>-2, Kyocera SN235P silicon nitride [100]



and lacking the glassy grain boundary phases typically present in commercially supplied alumina [135, 151–153]. These materials are not representative of commercially available alumina, and so are not included here. At room temperature, elimination of H<sub>2</sub>O from the test environment, such as by testing in vacuum, leads to a significant increase in the flexural strength of alumina by eliminating slow crack growth [150]. Reported values of flexural strength of sintered AlN are very sparse in the literature, but quite a large number of RT flexural strength data are available for hot pressed AlN, and these are presented in Fig. 6, along with the data for the other materials reviewed.

High-temperature flexural strength data for AlN are very scarce. AlN typically has an RT strength intermediate to that of alumina and beryllia. Some relatively high values, above 390 MPa, for RT flexural strength of AlN have been reported, mostly for polished specimens [154, 155], or electronic substrates [26, 27]. De With and Hattu [104] measured a dependence of flexural strength of hot pressed AlN on surface roughness, with flexural strength decreasing significantly for a greater surface roughness for a hot pressed AlN, from 310 MPa for surface finish  $R_a = 0.2 \mu\text{m}$ , decreasing to 237 MPa for  $R_a = 1.1 \mu\text{m}$ . Other studies reporting the variation of RT flexural strength with surface condition for AlN are also reviewed by De With and Hattu [104]. However, the high strength values reported for polished specimens are not representative of commercially available structural AlN bodies. Y<sub>2</sub>O<sub>3</sub> has

been found to be an effective additive for producing high density, high strength sintered AlN, while Sm<sub>2</sub>O<sub>3</sub> or La<sub>2</sub>O<sub>3</sub> have been shown to result in still higher strengths, in excess of 400 MPa [156].

Reported experimental values for the flexural strength of BeO at room temperature and elevated temperatures are scarce [57]. The strength of BeO typically increases above room temperature, reaching a strength maximum between 500–1200 °C, and then decreases rapidly at higher temperatures [54, 57, 59, 150]. However, the maxima are not always observed. Porosity, or high additive or impurity contents, which can dominate the failure mode, can reduce or eliminate the strength maxima, giving a strength plateau at intermediate temperatures [150]. Fryxell and Chandler [59] reported the increase in strength from room temperature to the strength maximum at intermediate temperature to be larger, and occur at higher temperature, with increasing grain size. Carniglia et al. [54] ascribed the strength minima observed around room temperature in their three-point flexural strength tests of hot pressed BeO to chemisorbed moisture. Some authors have reported the strength of BeO measured in vacuum to be higher than when measured in air [157]. For a given porosity level the RT flexural strength of BeO increases with decreasing grain size. However, attainment of very high densification in BeO is only attainable by either hot pressing or by sintering at high temperatures, or for long isothermal hold times, resulting in large grain sizes and thus a reduction in

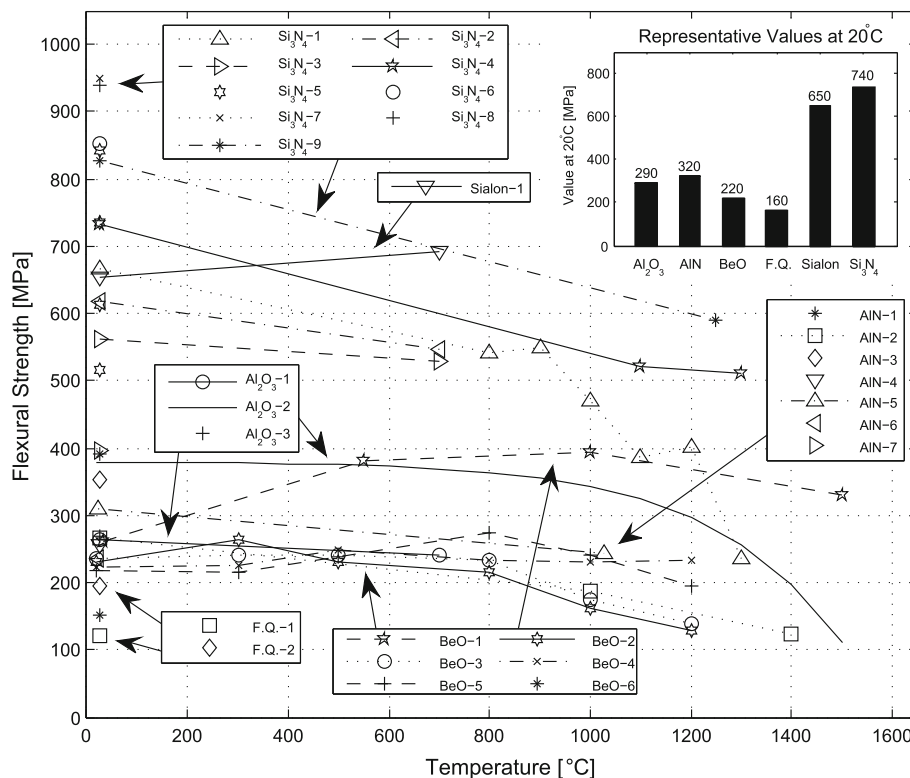


**Fig. 6** Flexural strength values from the following references: Al<sub>2</sub>O<sub>3</sub>-1, CoorsTek AD995 alumina [100]; Al<sub>2</sub>O<sub>3</sub>-2, review of alumina [17]; Al<sub>2</sub>O<sub>3</sub>-3, Wesgo AL995 alumina [161]; AlN-1, tape-cast, dry-pressed and sintered AlN [27]; AlN-2, HP AlN [37]; AlN-3, sintered AlN with 5 wt% Y<sub>2</sub>O<sub>3</sub> [156]; AlN-4, Keramont Corporation sintered AlN [136]; AlN-5, Cerac hot pressed AlN with  $R_a \approx 0.2 \mu\text{m}$  [104]; AlN-6, Cerac hot pressed AlN with  $R_a \approx 1.1 \mu\text{m}$  [104]; AlN-7, HP AlN [105]; BeO-1, high purity hot pressed BeO with 100%t.d. and 20  $\mu\text{m}$  grain size [54]; BeO-2, BeO from AOX powder, 2.90 g cm<sup>-3</sup>, 10  $\mu\text{m}$  grain size [59]; BeO-3, BeO From AOX Powder, 2.90 g cm<sup>-3</sup>, 20  $\mu\text{m}$  grain size [59]; BeO-4, BeO from UOX powder, 2.90 g cm<sup>-3</sup>, 10  $\mu\text{m}$  grain size [59]; BeO-5, BeO from UOX powder, 2.90 g cm<sup>-3</sup>, 20  $\mu\text{m}$

grain size [59]; BeO-6, sintered BeO from UOX Powder, 2.86 g cm<sup>-3</sup>, grain size 28  $\mu\text{m}$  [52]; F.Q.-1, KS-4V fused quartz [108]; F.Q.-2, KS-4V fused quartz [108]; Sialon-1, Kennametal TK4 sialon [100]; Si<sub>3</sub>N<sub>4</sub>-1, sintered silicon nitride [162]; Si<sub>3</sub>N<sub>4</sub>-2, Ceradyne Ceralloy 147-31N silicon nitride [100]; Si<sub>3</sub>N<sub>4</sub>-3, Kyocera SN235P silicon nitride [100]; Si<sub>3</sub>N<sub>4</sub>-4, GTE Laboratories PY6 HIP silicon nitride [141]; Si<sub>3</sub>N<sub>4</sub>-5, sinter-reaction-bonded silicon nitride [94]; Si<sub>3</sub>N<sub>4</sub>-6, 98%t.d. pressureless sintered Si<sub>3</sub>N<sub>4</sub> with 5 wt% MgO and 3 wt% Y<sub>2</sub>O<sub>3</sub> [97]; Si<sub>3</sub>N<sub>4</sub>-7, 99%t.d. pressureless sintered Si<sub>3</sub>N<sub>4</sub> with 5 wt% MgO and 4 wt% Y<sub>2</sub>O<sub>3</sub> [97]; Si<sub>3</sub>N<sub>4</sub>-8, 98%t.d. pressureless sintered Si<sub>3</sub>N<sub>4</sub> with 5 wt% MgO and 5 wt% Y<sub>2</sub>O<sub>3</sub> [97]; Si<sub>3</sub>N<sub>4</sub>-9, AlliedSignal GN-10 HIP Si<sub>3</sub>N<sub>4</sub> [163]

strength. Clare [53] found that fine grain sizes in low-porosity sintered BeO could only be attained with powders with low Fe impurity. Hot pressing of BeO typically results in higher densification for a given final grain size than pressureless sintering, and this results in higher strength. For pressureless sintering, an optimal compromise between densification and grain size is typically found in the grain size range 5–20  $\mu\text{m}$ , with relative density  $\geq 95\%$  [49, 59]. Even still, the typical flexural strength of BeO is lower than that of the other ceramics considered in this study, with some RT values as low as 100–150 MPa reported [49, 52]. Typical RT values given by suppliers of commercially available sintered BeO are given in the range 175–275 MPa, although these values are unsubstantiated in the formal literature. Flaws limiting the strength of sintered BeO include areas of high porosity and fine grain size, areas of coarse grain size resulting from high Fe content,

areas of coarse grain size resulting from segregated impurities of Al, Mg, and Si, and very large elongated grains up to 200  $\mu\text{m}$  in length [53].

$\beta'$ -sialon typically has a bimodal equiaxed-acicular microstructure with interlocking grains leading to high-RT flexural strength, increasing with more pronounced acicular grain structure [85]. The typical RT flexural strength of duplex  $\alpha'/\beta'$ -sialons is also high, due to the presence of elongated  $\beta'$ -grains. The RT strength of many single-phase  $\alpha'$ -sialons, which typically have an equiaxed grain structure, is significantly less than those of  $\beta'$ -sialons ( $\approx 400$  MPa [158]). The flexural strength of  $\alpha'$ -sialons may be improved by promoting the formation of elongated grains, by careful selection of starting composition and control of sintering conditions, or use of elongated seed crystals in the starting powder [81, 159, 160]. Glassy oxynitride grain boundary phases in sialon result from reaction of sintering aids for

liquid-phase sintering to promote densification, and the oxide layer on silicon nitride powders [78]. Softening of the grain boundary phase at elevated temperatures leads to a reduction in strength. Reduced grain boundary phase in  $\alpha'$ -sialons leads to retention of flexural strength up to higher temperatures [71].

The flexural strength and fracture toughness of silicon nitride is higher than most other monolithic ceramics, due in part to the presence of interlocking elongated  $\beta$ - $\text{Si}_3\text{N}_4$  grains, resulting in an in situ reinforced microstructure [81]. This self-reinforced microstructure, consisting of small, mainly equiaxed grains, and large elongated interlocking grains—analogueous to whisker or fiber-reinforced ceramic composites [81]—leads to cracks propagating through the intergranular films, preventing intragranular fracture, leading to crack bridging by the elongated grains [81]. Sintering aids added to facilitate liquid-phase sintering may react with oxygen in the  $\text{Si}_3\text{N}_4$  powder and form glassy intergranular films, which significantly affect the material's strength, both at room temperature and elevated temperatures. The composition of the intergranular films are mainly determined by the sintering aids added. The intergranular glass affects the densification of silicon nitride and growth of the elongated  $\beta$ - $\text{Si}_3\text{N}_4$  grains during sintering. The flexural strength of  $\text{Si}_3\text{N}_4$  typically decreases in a gradual monotonic fashion with increasing temperature up to  $\approx 800$ – $1200$  °C, although some strength increases with temperature have been reported, especially in RBSN [150]. Experimental studies reporting high-temperature strength of silicon nitride typically do not report strength at intermediate temperatures, so interpolation from room temperature strengths over a large temperature difference must often be used. At higher temperatures, the strength of silicon nitride falls off more rapidly. The hot strength of  $\text{Si}_3\text{N}_4$  and sialon is dependent upon the grain boundary phase, which softens at elevated temperatures leading to a decrease in strength. The properties of the grain boundary phase, including the volume fraction, crystallinity, composition, and subsequent viscosity and glass transition temperature—all primarily determined by sintering aid addition—control the hot strength of  $\text{Si}_3\text{N}_4$ . Silicon nitride hot pressed with minimal sintering aids results in a very small volume fraction of grain boundary phase, leading to higher RT strength and retention of strength up to higher temperatures than for sintered silicon nitride. Use of  $\text{MgO}$  and  $\text{Y}_2\text{O}_3$  sintering aids in combination has been found to result in good densification and high-flexural strength [97].

### Tensile strength

Tensile strength measurements of structural ceramics, particularly at elevated temperatures are very sparse in the literature. Tensile strength measurements of ceramics typically provide greater accuracy than flexure tests, but are

often disfavored due to prohibitively higher costs [136]. Tensile ( $\sigma_t$ ) and flexural ( $\sigma_f$ ) strengths can be related using Weibull scaling [164], where details of the dimensions of the flexural and tensile test specimens, but not the flaw size, are required [105]:

$$\sigma_f = \sigma_t \left( \frac{v_t}{v_f} \right)^{\frac{1}{m}} \quad (19)$$

where  $v_t$  and  $v_f$  are the effective volume of the tensile and flexural specimens, respectively, and  $m$  is the Weibull modulus of the tensile specimens. In the flexural test, the effective stressed volume is smaller, so the flaw population which could initiate failure is smaller. Toutanji et al. [105] note that a conventional set of bend tests of 10–30 specimens could thus miss critical flaw populations such as agglomerates, which a tensile test—interrogating a much larger stressed volume—would not miss. Thus, calculating flexural strengths from tensile strength data by Weibull scaling yields conservative values for flexural strength; but calculating tensile strengths from flexural strength data leads to an over-estimation of tensile strength [99, 105].

Data for  $\sigma_t$  of all materials are plotted in Fig. 7.

Having considered flexural and tensile strength, it is interesting to note that very little data are available for compressive strength of the materials considered in this study, particularly at elevated temperatures. Data obtained are plotted in Fig. 8.

## Thermal material properties

### Specific heat capacity

Specific heat capacity, considered here at constant pressure ( $c_p$ ), is not strongly sensitive to microstructural or compositional differences. For multi-phase compounds,  $c_p$  may be accurately estimated from mass fraction weighted averaging of  $c_p$  of the constituent phases. The effect of large additions of sintering aids on  $c_p$  may thus be quantified. Beryllia, composed of low atomic mass atoms, has a much higher specific heat capacity than the other ceramics considered in this study. For fused quartz, the data provided by Kelley [168] are taken as the recommended curve up to 2000 K, interpolated back to 0 °C, being in excellent agreement with the data of Sosman [99] in this temperature range [169].

Data for  $c_p$  of all materials are plotted in Fig. 9.

### Thermal conductivity

The thermal conductivity of a crystalline electrically insulating solid may be calculated from [176, 177]:

**Fig. 7** Tensile strength values from the following references: Al<sub>2</sub>O<sub>3</sub>-1, CoorsTek AD995 alumina [100]; Al<sub>2</sub>O<sub>3</sub>-2, review of alumina [17]; AlN-1, HP AlN [105]; AlN-2, Keramont sintered AlN [136]; BeO-1, HP BeO [165]; Sialon-1, Kennametal TK4 sialon [100]; Si<sub>3</sub>N<sub>4</sub>-1, Ceradyne Ceralloy 147-31N silicon nitride [100]; Si<sub>3</sub>N<sub>4</sub>-2, Kyocera SN235P silicon nitride [100]; Si<sub>3</sub>N<sub>4</sub>-3, GTE Laboratories PY6 HIP silicon nitride [141]; Si<sub>3</sub>N<sub>4</sub>-4, sintered silicon nitride [162]; Si<sub>3</sub>N<sub>4</sub>-5, Allied Signal GN-10 silicon nitride [166]

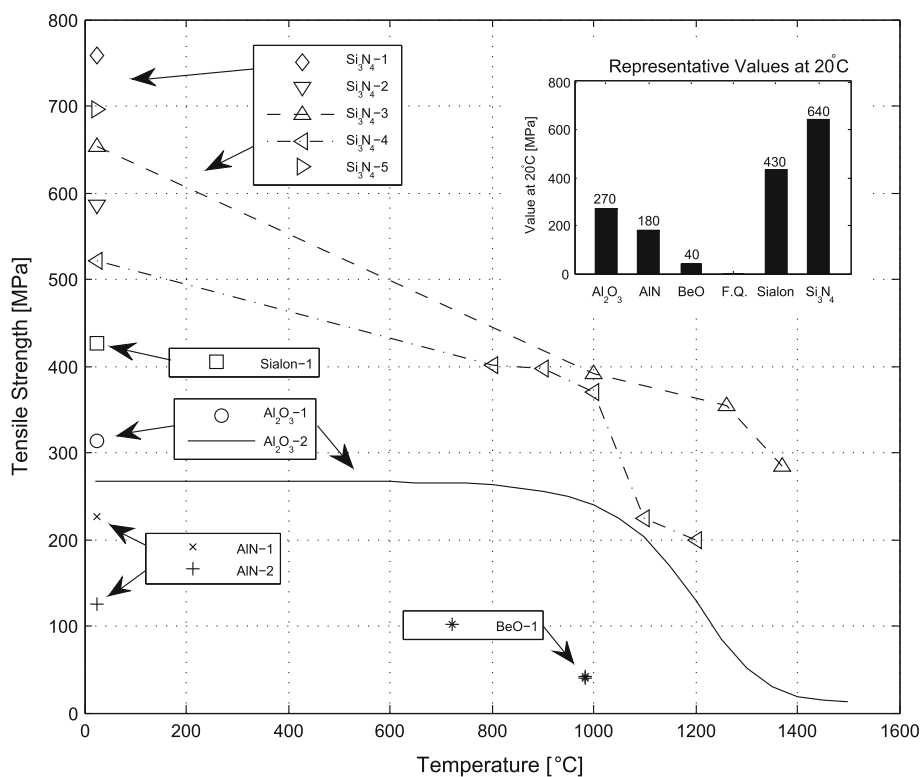
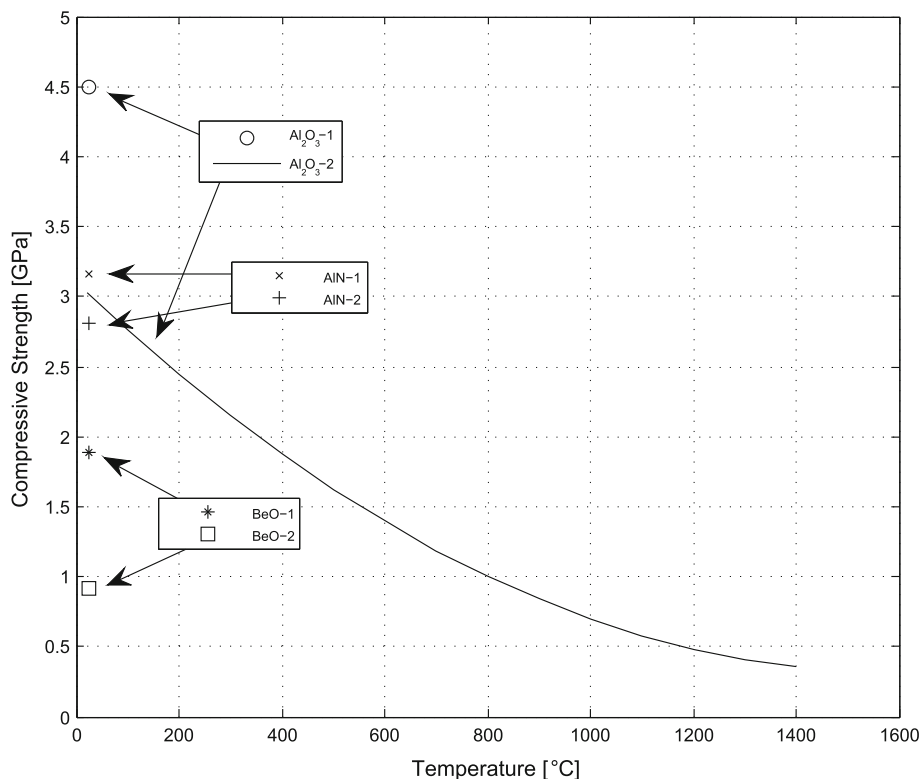


**Fig. 8** Compressive strength values from the following references: Al<sub>2</sub>O<sub>3</sub>-1, hot pressed Al<sub>2</sub>O<sub>3</sub> [60]; Al<sub>2</sub>O<sub>3</sub>-2, review of alumina [17]; AlN-1, hot pressed AlN [60]; AlN-2, hot pressed AlN [167]; BeO-1, cold pressed and sintered BeO [60]; BeO-2, hot pressed BeO [60]

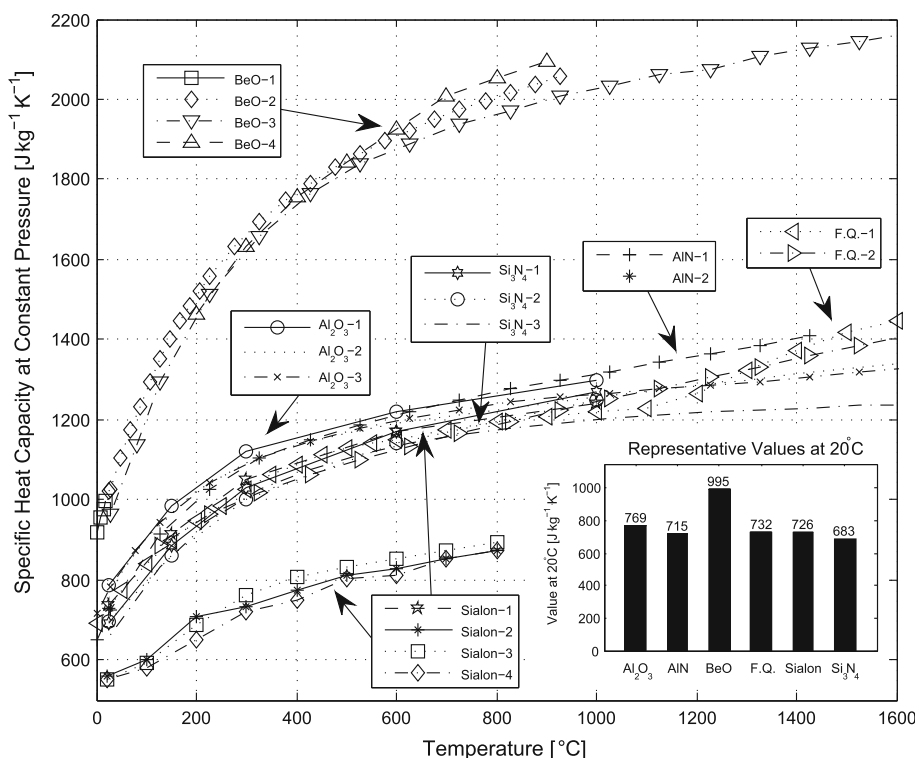


$$\lambda = \frac{1}{3} \bar{\rho} \bar{c}_V l_{ph} v_{ph} \quad (20)$$

where  $\bar{\rho}$  is the molar density ( $\text{kg mol}^{-1}$ ),  $\bar{c}_V$  is the molar specific heat capacity at constant volume ( $\text{J mol}^{-1} \text{K}^{-1}$ ),

$l_{ph}$  is the phonon mean free path (m), and  $v_{ph}$  is the mean phonon velocity ( $\text{m s}^{-1}$ ), which is approximately independent of temperature. The phonon mean free path is affected by intrinsic phonon-phonon scattering, which is

**Fig. 9** Specific heat capacity values from the following references: Al<sub>2</sub>O<sub>3</sub>-1, CoorsTek AD995 alumina [100]; Al<sub>2</sub>O<sub>3</sub>-2, review of alumina [17]; Al<sub>2</sub>O<sub>3</sub>-3, review of alumina [170]; AlN-1, theoretical calculation for AlN [144]; AlN-2, theoretical calculation for AlN [171]; BeO-1, 99.6% pure BeO [172]; BeO-2, 99.96% pure BeO [173]; BeO-3, theoretical calculation for BeO [174]; BeO-4, beryllia [175]; F.Q.-1, review of vitreous silica [99]; F.Q.-2, review of vitreous silica [168]; Sialon-1, Kennametal TK4 sialon [100]; Sialon-2, 100 wt% β-sialon [78]; Sialon-3, 5 wt% α-, 95 wt% β-sialon [78]; Sialon-4, 20 wt% α-, 80 wt% β-sialon [78]; Si<sub>3</sub>N<sub>4</sub>-1, Ceradyne Ceralloy 147-31N silicon nitride [100]; Si<sub>3</sub>N<sub>4</sub>-2, Kyocera SN235P silicon nitride [100]; Si<sub>3</sub>N<sub>4</sub>-3, theoretical calculation for β-Si<sub>3</sub>N<sub>4</sub> [90]



temperature dependant, and extrinsic phonon scattering at defects, grain boundaries, and other crystal imperfections, which is approximately independent of temperature [177]. At very low temperatures, phonon-phonon scattering is negligible, resulting in  $\lambda$  scaling with  $\bar{c}_V$ , which scales as  $T_{abs}^3$ . At low temperatures the average mean free path is dominated by extrinsic scattering [177]. Phonon-phonon scattering increases with increasing temperature, decreasing the phonon mean free path [177]. The thermal conductivity thus reaches a maximum at low temperatures, typically 30–150 K, and thereafter decreases with increasing temperature. At room temperatures, phonon scattering at grain boundaries is negligible, and is dominated by scattering at crystal lattice imperfections such as dislocations and point defects [110, 178]. At intermediate temperatures, phonon-phonon interactions become the dominant factor in determining the thermal conductivity in ceramics, as phonon-phonon scattering increases with temperature [177]. At high temperature  $\bar{c}_V$  approaches a constant value—the Dulong-Petit limit—but the mean free path due to phonon-phonon scattering decreases exponentially, approximately scaling by  $1/T_{abs}$ , causing the thermal conductivity to scale approximately with  $1/T_{abs}$  [176, 179], or thermal resistivity to be linearly dependent upon  $T_{abs}$ . Deviations from  $1/T_{abs}$  scaling have, however, been noted for some materials [58]. At very high temperatures the effect of thermal radiation within ceramics becomes important, becoming very significant above 1500 K [180]. At these very high temperatures the thermal conductivity

can approach a constant or even increase [180]. For ceramics, large scatter exists in reported values of room temperature thermal conductivity, due to sensitivity of RT thermal conductivity to variations in composition, impurity levels, processing, resulting microstructure [177], and measurement method [180]. The scatter for each material progressively reduces at elevated temperatures, as intrinsic phonon scattering mechanisms controlling thermal conductivity become more dominant, leading to a reduction in sensitivity of thermal conductivity to microstructural or compositional differences [177].

The presence of porosity significantly reduces the RT thermal conductivity of ceramics, due to a reduction in conduction pathways. Thermal conductivity decreases with increasing porosity. Several relations have been proposed to extrapolate thermal conductivity measurements to thermal conductivity at zero porosity, including that of Kingery et al. [181]:

$$\lambda_0 = \frac{\lambda_{meas}}{1 - P} \tag{21}$$

where  $P$  is the porosity (pore volume fraction),  $\lambda_{meas}$  is the measured thermal conductivity, and  $\lambda_0$  is the calculated thermal conductivity for zero porosity. However, the relationship between conductivity and porosity is non-linear, and Eq. 21 cannot be used over large variations in porosity [58]. RT thermal conductivity can also be reduced by the presence of thick, or low thermal conductivity grain boundary phases, or by grain defects.

The thermal conductivity of sintered or hot pressed alumina is lower than that of single-crystal alumina (sapphire), with thermal conductivity decreasing with increasing porosity. Typical RT thermal conductivity of sintered  $\text{Al}_2\text{O}_3$  with  $\geq 98\%$  and  $\geq 99.5\%$  purity, is  $\approx 32 \text{ W m}^{-1} \text{ K}^{-1}$  (compared to  $\approx 42 \text{ W m}^{-1} \text{ K}^{-1}$  typical for sapphire [101]).

At room temperature, oxygen-related defects are the dominant mechanism limiting the thermal conductivity of AlN [22, 40], but their effect decreases at elevated temperatures [24]. Metallic impurities also have the effect of greatly reducing the RT thermal conductivity [38]. Above 1000 K thermal conductivity is governed by anharmonicity [182], leading to the high-temperature thermal conductivity of AlN being independent of ceramic purity. Due to the high dependency upon oxygen-related defects, a wide spread exists in the data reported for RT thermal conductivity of AlN. The thermal conductivity of AlN hot pressed without additives is comparatively low—typically in the range  $30\text{--}70 \text{ W m}^{-1} \text{ K}^{-1}$  [25, 37]—due to the effects of lattice defects (Al vacancies) resulting from dissolved oxygen impurity. For a given oxygen impurity level, the type and amount of sintering aid added has the greatest effect on AlN thermal conductivity [25].

Yttria, the most commonly used sintering aid for AlN, and other rare-earth oxides, including  $\text{Sm}_2\text{O}_3$ ,  $\text{Nd}_2\text{O}_3$ , and  $\text{Pr}_2\text{O}_3$ , have been shown to produce near-theoretical density AlN, with high thermal conductivity [25]. The sintering aid CaO has been shown to produce lower thermal conductivity AlN but has a reduced powder cost [183]. The thermal conductivity of yttria-doped AlN increases with dopant addition, as yttria reacts with oxygen to reduce the defect concentration in AlN grains, up to a peak thermal conductivity value [25]. With even greater yttria addition, the increasing yttrium aluminate grain boundary phase thickness reduces the bulk thermal conductivity. Achievement of high thermal conductivity thus requires optimization of the amount of sintering aid added, with addition of an approximately equimolar amount of  $\text{Y}_2\text{O}_3$  to the  $\text{Al}_2\text{O}_3$  content of the AlN powder, resulting in very high thermal conductivity [25]. The thermal conductivity of AlN doped with rare-earth oxides has also been shown to increase with annealing: increasing with longer annealing times and higher annealing temperatures, with an attendant increase in grain size [25].

Irradiation of AlN at room temperature with ultraviolet light has been shown to reversibly reduce its thermal conductivity due to increased phonon scattering cross section, the original thermal conductivity returning when irradiated with visible light [184, 185]. The inner surface of the GCT will be exposed to high levels of UV radiation from the helicon plasma during operation. However, the effect, which is inversely related to sample thickness,

becomes negligible for structurally sized components, and is thus neglected in this study.

For AlN, due to the scarcity of high-temperature experimental measurements of thermal conductivity, a simple extrapolation up to  $1400 \text{ }^\circ\text{C}$  may be made using  $1/T_{\text{abs}}$  scaling.

Beryllia exhibits the highest RT thermal conductivity of any ceramic, although this decreases rapidly above room temperature, dropping below that of AlN at intermediate temperatures. At very high temperatures a slight increase in thermal conductivity of BeO has been measured [58].

Theoretical analysis of the thermal conductivity of fused quartz—which increases above room temperature in a non-linear manner, in contrast to (crystalline) ceramics—has proved difficult [186]. Radiation heat transfer becomes significant in the measurement of thermal conductivity of fused quartz above  $\approx 300 \text{ }^\circ\text{C}$  [169]. The compound effects of conduction and radiation through the material may be considered as one, as the effective thermal conductivity  $\lambda^*$ , or the effects of radiation may be corrected for, yielding the true thermal conductivity  $\lambda$ . A divergence thus exists for reported literature values around this temperature, which becomes very significant at high temperatures, with different studies variously reporting the real or effective thermal conductivity [186]. The radiant component of heat transfer varies with sample thickness—resulting in higher measured values of  $\lambda^*$  in thicker samples—and composition [169]. In addition, determination of the correct values of thermal conductivity for fused quartz is complicated by the fact that, despite the large number of experimental studies, few of these specify the origin, or purity of the samples tested [99, 169].

$\alpha'$ -sialon has lower thermal conductivity than  $\beta'$ -sialon due to shorter phonon mean free path, resulting from greater lattice asymmetry, and complexity resulting from inclusion of metal cations [78]. Duophase ( $\alpha' + \beta'$ )-sialons have thermal conductivities intermediate to those of  $\alpha'$ - and  $\beta'$ -sialon, with thermal conductivity increasing with  $\beta'$ -phase content [78].

$\beta$ - $\text{Si}_3\text{N}_4$  has high intrinsic thermal conductivity [177, 178, 187–190], with reported thermal conductivities for  $\beta$ - $\text{Si}_3\text{N}_4$  as high as  $162 \text{ W m}^{-1} \text{ K}^{-1}$  [191]. The intrinsic thermal conductivity of  $\alpha$ - $\text{Si}_3\text{N}_4$  is lower than that of  $\beta$ - $\text{Si}_3\text{N}_4$ , due to the higher complexity of its crystal structure [189], with thermal conductivity of silicon nitride ceramics increasing with increasing  $\beta$ -phase content [91, 192].

Selection of type and concentration of additive greatly affects the thermal conductivity and porosity of sintered  $\text{Si}_3\text{N}_4$ . Typical sintering aids used for the densification of silicon nitride are yttria, alumina and magnesia, and rare-earth oxides either singly or in combination [193], with yttria being found to be effective in producing higher

thermal conductivity silicon nitride [91]. The presence of Al ions as impurity or additive affects the thermal conductivity, by Al and O ions forming a solid solution— $\beta'$ -sialon—in the  $\beta$ - $\text{Si}_3\text{N}_4$  grains, leading to increased phonon scattering and thus lower thermal conductivity [177, 192], causing silicon nitride produced with  $\text{Al}_2\text{O}_3$  sintering aid to have low thermal conductivity.  $\text{Y}_2\text{O}_3$  or  $\text{MgO}$  dopants form only secondary phases, and not solid solutions in the  $\text{Si}_3\text{N}_4$  grains [177], leading to higher sintered thermal conductivities than with  $\text{Al}_2\text{O}_3$  addition.

Thick glassy grain boundaries can reduce the thermal conductivity of silicon nitride, due to the lower thermal conductivity of the glassy phase, but for silicon nitrides with low secondary phase content, grain boundary thickness is not the main controlling factor on thermal conductivity [91].

Room temperature thermal conductivity of silicon nitride is not controlled by grain size, with large increases in grain size only slightly increasing the thermal conductivity [110], particularly for  $\text{Al}_2\text{O}_3$ -doped  $\text{Si}_3\text{N}_4$  [91]. Instead, the RT thermal conductivity is controlled by the amount of structural defects, such as dislocations and point defects, which cause phonon scattering [91]. Although high thermal conductivities have been reported for  $\text{Y}_2\text{O}_3$ -doped  $\text{Si}_3\text{N}_4$  with large  $\beta$ - $\text{Si}_3\text{N}_4$  grains [194, 195], the higher thermal conductivity is due to reduced structural defect density in the larger grains [91]. The thermal conductivity of  $\beta$ - $\text{Si}_3\text{N}_4$  crystals is anisotropic [196]. Very high (and macroscopically anisotropic) thermal conductivities have been achieved for silicon nitrides with large oriented elongated  $\beta$ -phase grains, resulting from anisotropic processing techniques (extrusion [191], hot pressing [110], tape-casting [178, 197]), and in some cases by also seeding with  $\beta$ - $\text{Si}_3\text{N}_4$  crystals.

Processing details, including sintering temperature [91] also strongly affect the resultant microstructure, and thus the thermal conductivity. Attainment of high thermal conductivity requires the use of high purity starting powders with low oxygen content and low cationic impurities, full densification of the sintered body, and the optimization of many factors including sintering parameters [91] and sintering aid(s). Very high thermal conductivity  $\text{Si}_3\text{N}_4$  has been reported in many studies [94, 191, 198–200], produced by careful control of purity and oxygen content of raw powders [94, 201], selection of additives [202], control of microstructure morphology and grain size [109, 178, 194, 197, 203, 204], and use of  $\beta$ - $\text{Si}_3\text{N}_4$  seed crystals [205]. However, despite the large volume of studies reporting techniques for production of high thermal conductivity silicon nitride, typical commercially available silicon nitride [206] at present has a far lower thermal conductivity. As the thermal conductivity of these experimental materials does not reflect what is commercially available,

they will not be considered for the purposes of determining the most representative set of commercially available material values in the current analysis.  $\text{Si}_3\text{N}_4$  with thermal conductivities in excess of  $45 \text{ W m}^{-1} \text{ K}^{-1}$  are not commonly commercially available, typical values being in the range  $15\text{--}42 \text{ W m}^{-1} \text{ K}^{-1}$ . Typical high-purity commercial  $\text{Si}_3\text{N}_4$  powders contain  $\approx 1 \text{ wt}\%$  oxygen [94], and metallic impurities [91], limiting the attainable thermal conductivity. The coarse microstructures typically present in high thermal conductivity  $\text{Si}_3\text{N}_4$ , resulting from promotion of grain growth, significantly impacts on the material's strength [94, 110, 207], reducing the suitability of these materials for structural applications. Although these materials are not typically commercially available, the volume of ongoing research in this field will likely lead to these high thermal conductivity materials becoming commercially available in the coming years, broadening the spectrum of applications for silicon nitride. Data obtained for the thermal conductivity of all materials are plotted in Fig. 10.

#### Thermal expansion coefficient

Accurate knowledge of thermal expansion coefficients at elevated temperatures is critical for material processing [211] and prediction of thermal stresses for mechanical design. The rate of change of specific volume of most materials typically increases with increasing temperature [211], leading to increasing issues of thermal stress at elevated temperatures. The dilation of a material with temperature may be characterized by the rate of change of a linear dimension of the material, referred to the instantaneous length of that dimension, termed the true instantaneous coefficient of thermal expansion (COTE),  $\alpha'$  such that:

$$\alpha' = \frac{1}{L_T} \frac{\partial L}{\partial T} \quad (22)$$

where  $L_T$  is the length of the specimen at temperature  $T$ . A more commonly used procedure [99] is to express thermal dilation as the rate of change of linear dimension with temperature, referred to the specimen's linear dimension at some reference temperature, such as 0 or  $25 \text{ }^\circ\text{C}$ :

$$\alpha = \frac{1}{L_0} \frac{\partial L}{\partial T} \quad (23)$$

where  $L_0$  is the linear dimension at the reference temperature. As the absolute change in dimension of the specimen will be very small, the instantaneous COTE referred to a reference temperature ( $\alpha$ ) will be an excellent approximation to the true instantaneous COTE ( $\alpha'$ ). Thermal dilation is also commonly expressed as an average coefficient of thermal expansion between a

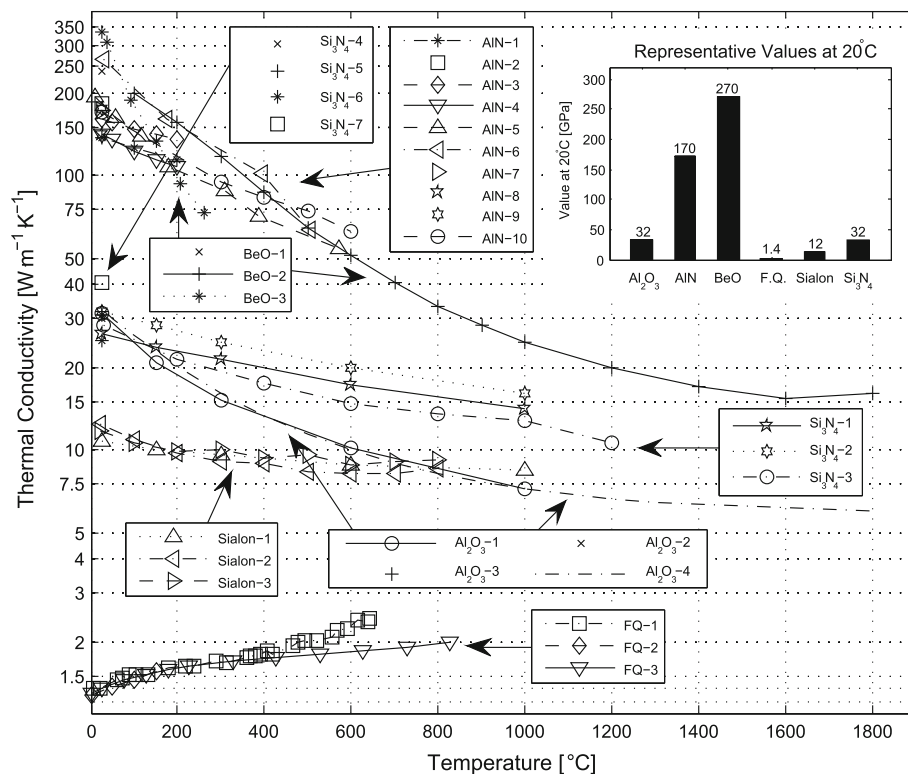


**Fig. 10** Thermal conductivity values. Al<sub>2</sub>O<sub>3</sub>-1, CoorsTek AD995 alumina [100]; Al<sub>2</sub>O<sub>3</sub>-2, CoorsTek AD998 alumina [101]; Al<sub>2</sub>O<sub>3</sub>-3, Wesgo AL998 alumina [101]; Al<sub>2</sub>O<sub>3</sub>-4, review of alumina [17]; AlN-1, tape-cast, dry-pressed and sintered AlN [27]; AlN-2, sintered AlN 2.9 wt% Y<sub>2</sub>O<sub>3</sub> [44]; AlN-3, hot pressed AlN substrate [26]; AlN-4, sintered AlN substrate [26]; AlN-5, sintered AlN, 2.2 wt% oxygen impurity [182]; AlN-6, sintered AlN, 0.05 wt% oxygen impurity [182]; AlN-7, sintered AlN 5 wt% Y<sub>2</sub>O<sub>3</sub>, 0.8 wt% O [156]; AlN-8, sintered AlN 1 mol% Y<sub>2</sub>O<sub>3</sub> [103]; AlN-9, sintered AlN 4.91 wt% Y<sub>2</sub>O<sub>3</sub> [25]; AlN-10, sintered AlN 4 wt% Y<sub>2</sub>O<sub>3</sub> [25]; BeO-1, Brush-Wellman 995 BeO [101]; BeO-2, 95%t.d. BeO [58]; BeO-3, sintered

un-doped BeO, 2.86 g cm<sup>-3</sup> [52]; F.Q.-1, 99.97% pure fused quartz [186]; F.Q.-2, fused quartz [208]; F.Q.-3, review of fused quartz [169]; Sialon-1, Kennametal TK4 sialon [100]; Sialon-2,  $\beta$ -sialon [78]; Sialon-3, 20%  $\alpha$ -, 80%  $\beta$ -sialon [78]; Si<sub>3</sub>N<sub>4</sub>-1, Ceradyne Ceralloy 147-31N silicon nitride [100]; Si<sub>3</sub>N<sub>4</sub>-2, Kyocera SN235P silicon nitride [100]; Si<sub>3</sub>N<sub>4</sub>-3, nitrated pressureless sintered silicon nitride [209]; Si<sub>3</sub>N<sub>4</sub>-4, Ceramic for industry CFI3208 silicon nitride [206]; Si<sub>3</sub>N<sub>4</sub>-5, Kyocera SN235P silicon nitride [206]; Si<sub>3</sub>N<sub>4</sub>-6, Honeywell GS44 silicon nitride [206]; Si<sub>3</sub>N<sub>4</sub>-7, Honeywell AS800 silicon nitride [206]

reference temperature, such as 0 or 25 °C, and a specified higher temperature:

$$\bar{\alpha} = \frac{1}{L_0} \frac{L - L_0}{T - T_0} \quad (24)$$

where  $L_0$  is the linear dimension at the reference temperature  $T_0$ . Care must be taken when dealing with COTE data, to distinguish between values of instantaneous and average COTE. Thermal dilation may also be more fundamentally defined in terms of rate of change of volume with respect to temperature, with corresponding definitions for volumetric true instantaneous COTE, instantaneous COTE referred to a reference temperature, and average COTE, respectively:

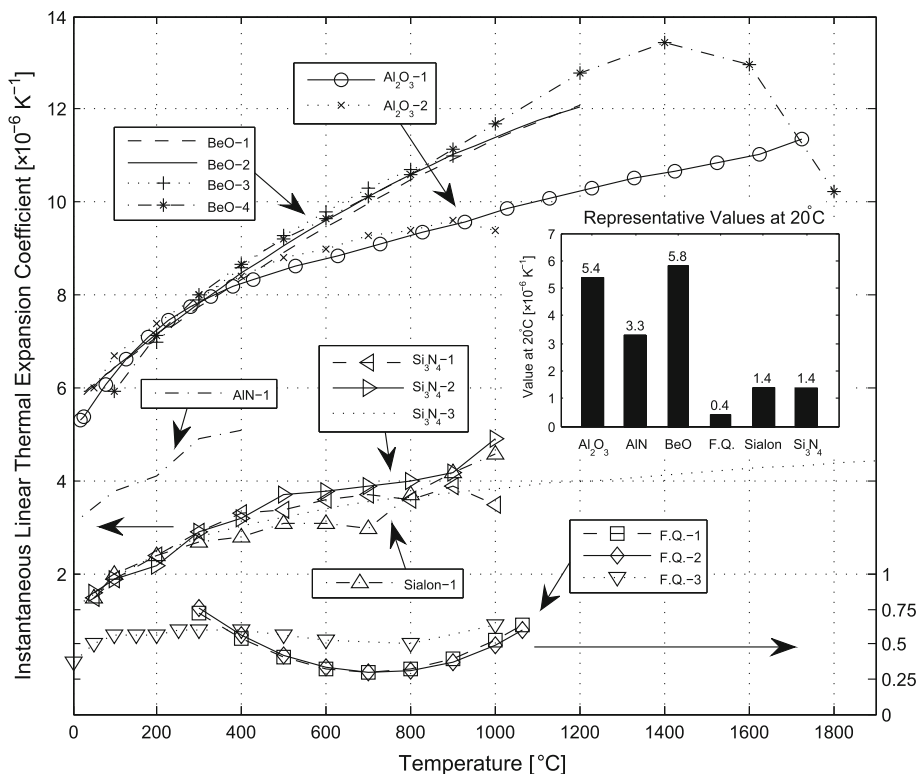
$$\beta' = \frac{1}{V_T} \frac{\partial V}{\partial T} \quad (25)$$

$$\beta = \frac{1}{V_0} \frac{\partial V}{\partial T} \quad (26)$$

$$\bar{\beta} = \frac{1}{V_0} \frac{V - V_0}{T - T_0} \quad (27)$$

In experimental studies of thermal expansion of ceramics found in the literature, linear coefficients of expansion are more widely reported than volumetric coefficients, as linear variations in specimen dimension can be more easily measured than volumetric variations; although volumetric coefficients of thermal expansion are commonly found in the literature for computational physics studies of the structure of materials. For isotropic substances, the instantaneous linear COTE may be approximated by  $\alpha \cong \beta/3$  with only a small error, as the actual linear dilation will be small. Data from some sources reported as values of

**Fig. 11** Thermal expansion coefficient values from the following references: Al<sub>2</sub>O<sub>3</sub>-1, review of alumina [170]; Al<sub>2</sub>O<sub>3</sub>-2, CoorsTek AD995 alumina [100]; AlN-1, hot pressed AlN [26]; BeO-1, isostatically pressed and sintered BeO [59]; BeO-2, extruded and sintered BeO [59]; BeO-3, review of BeO [175]; BeO-4, review of BeO [58]; F.Q.-1, fused quartz from electrically melted quartz crystal powder [65]; F.Q.-2, fused quartz from flame fusion of quartz crystals [65]; F.Q.-3, review of vitreous silica [99]; Sialon-1, Kennametal TK4 sialon [100]; Si<sub>3</sub>N<sub>4</sub>-1, Ceradyne ceralloy 147-31N silicon nitride [100]; Si<sub>3</sub>N<sub>4</sub>-2, Kyocera SN235P silicon nitride [100]; Si<sub>3</sub>N<sub>4</sub>-3, theoretical calculation β-Si<sub>3</sub>N<sub>4</sub> [90]



instantaneous volumetric COTE have been used in this study, by utilizing this approximate relation. The rate of dilation of ceramics with respect to temperature is relatively independent of porosity, allowing thermal expansion coefficients to be calculated from lattice parameter measurements [210], with only slight error resulting from defects in the polycrystalline material [17]. The thermal expansion coefficient of non-cubic crystals is typically anisotropic [211], resulting in change in both shape (deformation) and volume (dilation) when heated [99]. Anisotropic thermal expansion of non-cubic lattice structures in polycrystalline materials can lead to thermal-stress-induced-cracking [211]. For crystals of the hexagonal lattice system the instantaneous thermal expansion coefficients along the *a* and *c* lattice directions are defined by:

$$\alpha_a = \frac{1}{a_T} \frac{\partial a}{\partial T} \approx \frac{1}{a_0} \frac{\partial a}{\partial T} \tag{28}$$

$$\alpha_c = \frac{1}{c_T} \frac{\partial c}{\partial T} \approx \frac{1}{c_0} \frac{\partial c}{\partial T} \tag{29}$$

The directionally averaged instantaneous thermal expansion coefficient of the corresponding polycrystalline material composed of randomly oriented grains is then:

$$\tilde{\alpha} = \frac{(2\alpha_a + \alpha_c)}{3} \tag{30}$$

Data from both X-ray diffraction of single-crystals and dilatometry are considered for the determination of the instantaneous linear COTE of the ceramics considered in

this study. The amorphous nature of fused quartz necessitates the sole use of dilatometry. For substances with the wurtzite crystal structure, such as AlN and BeO,  $\alpha_c$  is lower than  $\alpha_a$ , leading to a reduction in the *c/a* ratio with increasing temperature [145, 211, 212]. Some polycrystalline ceramics exhibit preferential grain orientation, typically resulting from processing such as extrusion, hot pressing, or tape-casting, leading to macroscopically anisotropic thermal expansion. BeO ceramics have been variously reported with macroscopically isotropic [58] and anisotropic [59] thermal expansion coefficients. The COTE of many but not all specimens of vitreous silica reported are very slightly anisotropic [99]. Due to the high purity of fused quartz, its thermal expansion coefficient can be significantly affected by small differences in composition [65]. The previous thermal history of a sample of fused quartz can greatly affect its measured thermal expansion coefficient, with significant differences noted between unannealed and fully annealed samples [65, 99]. The  $\alpha'$  and  $\beta'$ -phases of sialon have differing thermal expansion coefficients ( $\alpha_{\alpha'-\text{phase}} \approx 3.7\text{--}4.0 \times 10^{-6} \text{ K}^{-1}$  [71],  $\alpha_{\beta'-\text{phase}} \approx 3.2 \times 10^{-6} \text{ K}^{-1}$ ), causing residual stresses to develop in duophase sialons [75]. The thermal expansion coefficient of oxynitride glass ( $\alpha \approx 5.2\text{--}6.6 \times 10^{-6} \text{ K}^{-1}$ ) differs from that of both  $\alpha'$  and  $\beta'$ -sialon phases—affecting the bulk properties of the ceramic—and is dependent upon various factors, including nitrogen content and modifier cation, increasing N:O ratio resulting in a decrease in thermal

expansion coefficient due to increased cross-linking [79]. The thermal expansion coefficients of the  $\alpha$  and  $\beta$ -phases of  $\text{Si}_3\text{N}_4$  differ by only a very small amount [90].

Temperature-dependent data for the thermal expansion coefficients of all materials are given in Fig. 11.

## Conclusions

Representative material property data, given as a function of temperature where possible, have been gathered for constrained material specifications for alumina, aluminium nitride, beryllia, fused quartz, sialon, and silicon nitride. The material specifications have been chosen to best reflect advanced commercially available material grades. These data can be used by the design engineer in the preliminary stages of design for materials selection and simulation. Detailed design should always be supported by experimental verification of the material properties of the intended material.

It is clear from this study that more experimental studies of the tensile, flexural and compressive strengths are required as a function of temperature, for candidate structural ceramics for use in high-power plasma sources and other high-power dielectric applications. Further work is required to compile representative values for the dielectric properties of these materials, and to assess the resistance of these materials to the plasma environment in VASIMR®.

**Acknowledgements** The authors would like to acknowledge the financial support of the FÁS Science Challenge Programme, Ireland.

## References

- Chang-Diaz FR (2000) *Sci Am* 283(5):90
- Squire JP, Chang-Diaz FR, Glover TW, Jacobson VT, McCaskill GE, Winter DS, Baity FW, Carter MD, Goulding RH (2006) *Thin Solid Films* 506:579
- Batishchev O, Molvig K, Chang-Diaz FR, Squire JP (2003) In: 30th EPS conference on controlled fusion and plasma physics, St. Petersburg, 7–11 July 2003
- Stanton KT, Browne DJ, Mulcahy J (2006) In: High Power Electrical Propulsion Workshop, Ad Astra Rocket Company, Liberia
- Mulcahy JM, Browne DJ, Stanton KT, Chang-Diaz FR, Cassady L (2008) In: 5th European thermal-sciences conference, Eindhoven
- Mulcahy James M, Browne David J, Stanton Kenneth T, Chang Diaz Franklin R, Cassady Leonard D, Berisford Daniel F, Bengtson Roger D (2009) *Int J Heat Mass Trans* 52(9–10):2343
- Tanikawa T, Shinohara S (2006) *Thin Solid Films* 506:559
- Fu GS, Xu HJ, Wang SF, Yu W, Sun W, Han L (2006) *Physica B* 382(1–2):17
- Blackwell DD, Chen FF (1997) *Plasma Sour Sci Technol* 6(4):569
- Toki K, Shinohara S, Tanikawa T, Shamrai KP (2006) *Thin Solid Films* 506:597
- Chen H, Kallos E, Muggli P, Katsouleas TC, Gundersen MA (2009) *Plasma Sci IEEE Trans* 37(3):456
- Little CE (1990) In: IEE Colloquium on Gas discharges as coherent and incoherent light sources, London
- Loveland DG, Orchard DA, Zerrouk AF, Webb CE (1991) *Meas Sci Technol* 2(11):1083
- Heemstra D, White K (2010) U.S.A. Patent No. 7759600
- Huffman M, Sakthivel P, Zimmerman T, Noble T (2000) U.S.A. Patent No. 6082374
- Weibull WA (1951) *J Appl Mech Trans ASME* 18(3):293
- Munro RG (1997) *J Am Ceram Soc* 80(8):1919
- Borland W (1989) In: *Electronic materials handbook: packaging, vol 1*. ASM International, New York
- Heikkinen JA, Orivuori S, Linden J, Saarelma S, Heikinheimo L (1999) *IEEE Trans Dielectrical Insulation* 6(2):169
- Howlader MMR, Kinoshita C, Shiiyama K, Kutsuwada M (2002) *J Appl Phys* 92(4):1995
- Goulding RH, Zinkle SJ, Rasmussen DA, Stoller RE (1996) *J Appl Phys* 79(6):2920
- Slack Glen A, Tanzilli RA, Pohl RO, Vandarsande JW (1987) *J Phys Chem Solids* 48(7):641
- Okamoto M, Arakawa H, Oohashi M, Ogihara S (1989) *J Ceram Soc Jpn* 97(1132):1478
- Watari K, Nakano H, Urabe K, Ishizaki K, Cao SX, Mori K (2002) *J Mater Res* 17(11):2940
- Jackson TB, Virkar AV, More KL, Dinwiddie RB, Cutler RA (1997) *J Am Ceram Soc* 80(6):1421
- Kurokawa Y, Utsumi K, Takamizawa H, Kamata T, Noguchi S (1985) *Compon Hybrid Manuf Technol IEEE Trans* 8(2):247
- Kuramoto N, Taniguchi H, Aso I (1986) *Compon Hybrid Manuf Technol IEEE Trans* 9(4):386
- Miyashiro F, Iwase N, Tsuge A, Ueno F, Nakahashi M, Takahashi T (1990) *Compon Hybrid Manuf Technol IEEE Trans* 13(2):313
- Norton MG (1993) *Microelectron Int* 6(3):18
- Gosey MT, Lodge KJ, Logan EA (1991) *GEC J Resh* 8(3):137
- Harris J (1998) *JOM J Miner Metals Mater Soc* 50(6):56
- Lodge KJ, Sparrow JA, Perry ED, Logan EA, Goosey MT, Pedder DJ, Montgomery C (1990) *Compon Hybrid Manuf Technol IEEE Trans* 13(4):633
- La Spina L, Iborra E, Schellevis H, Clement M, Olivares J, Nanver LK (2008) *Solid-State Electron* 52(9):1359
- Lin Z, Yoon RJ (2005) In: *Proceedings of the international symposium on advanced packaging materials: processes, properties and interfaces*, Irvine
- Long G, Foster LM (1962) *J Electrochem Soc* 109(12):1176
- Rafaniello W (1992) In: *Technical Report Contract Number DAAL03-88-C-001*, U.S. Army Research Office, Ann Arbor
- Taylor KM, Lenie C (1960) *J Electrochem Soc* 107(4):308
- Kuramoto N, Taniguchi H, Numata Y, Aso I (1985) *J Ceram Assoc* 93(1081):517
- Ueno F, Horiguchi A, Kasori M, Shinozaki K, Tsuge A (1987) In: *IUPAC-CHEMRAWN VI, advanced materials for innovations in energy, transportation and communications*, Tokyo, 17–22 May 1987
- Harris JH, Youngman RA, Teller RG (1990) *J Mater Res* 5(8):1763
- Buhr H, Muller G, Wiggers H, Aldinger F, Foley P, Roosen A (1991) *J Am Ceram Soc* 74(4):718
- Slack GA (1973) *J Phys Chem Solids* 34(2):321
- Slack GA, Schowalter LJ, Morelli D, Freitas JA (2002) *J Cryst Growth* 246(3–4):287
- Sakai H, Katsuda Y, Masuda M, Ihara C, Kameyama T (2008) *J Ceram Soc Jpn* 116(4):566
- Watari Koji (2001) *J Ceram Soc Jpn* 109(1265):S7

46. Sachet JP, Laval JY, Lepoutre F, Boccara AC (1990) *J Phys Colloq* 51(C1):617
47. Mitra S, Dutta G, Dutta I (1995) *J Am Ceram Soc* 78(9):2335
48. Schultheiss T, Christina V, Cole M, Rathke J, Elliott T, Nguyen V, Phillips L, Preble J (1999) In: *Proceedings of the 1999 particle accelerator conference*, vol 2, New York
49. Hessinger PS, Styhr KH, Ryshkewitch E (1962) In: *Technical report. National Beryllia Corp., Haskell*
50. Snead LL, Zinkle SJ (2005) In: *Space technology and applications international forum—STAIF 2005*, vol 746, Albuquerque
51. Hamlyn-Harris C, Borthwick A, Fanthome J, Waldon C, Nightingale M, Richardson N (2009) *Fus Eng Des* 84(2–6):887
52. Beaver WW, Theodore JG, Bielawski CA (1964) *J Nucl Mater* 14:326
53. Clare TE (1964) *J Nucl Mater* 14:359
54. Carniglia SC, Johnson RE, Hott AC, Bentle GG (1964) *J Nucl Mater* 14:378
55. Bardsley J, Ridal A (1964) *J Nucl Mater* 14:368
56. Veevers K, Whatham JF, Wright WJ (1964) *J Nucl Mater* 14:395
57. Brown RJ, Bass NW (1964) *J Nucl Mater* 14:341
58. Lillie J (May 19 1961) In: *Technical Report UCRL-6457. Lawrence Radiation Laboratory, University of California, Livermore*
59. Fryxell RE, Chandler BA (1964) *J Am Ceram Soc* 47(6):283
60. Heard HC, Cline CF (1980) *J Mater Sci* 15(8):1889. doi:[10.1007/BF00550614](https://doi.org/10.1007/BF00550614)
61. Kelly JW (1963) *J Nucl Mater* 8(2):227
62. Alexander CS, Chhabildas LC, Reinhart WD, Templeton DW (2008) *Int J Impact Eng* 35(12):1376
63. Shikama T, Yasuda K, Yamamoto S, Kinoshita C, Zinkle SJ, Hodgson ER (1999) *J Nucl Mater* 271:560
64. Gorshkov A, Orlinski D, Sannikov V, Vukolov K, Goncharov S, Sadovnikov Y, Kirillov A (1999) *J Nucl Mater* 273(3):271
65. Oishi J, Kimura T (1969) *Metrologia* 5(2):50
66. Jack KH, Wilson WI (1972) *Nat Phys Sci* 238(80):28
67. Oyama Y, Kamigaito O (1971) *Jpn J Appl Phys* 10(11):1637
68. Jack KH (1973) *Trans J Br Ceram Soc* 72(8):376
69. Oyama Y (1972) *Jpn J Appl Phys* 11(5):760
70. Jack KH (1976) *J Mater Sci* 11(6):1135. doi:[10.1007/BF02396649](https://doi.org/10.1007/BF02396649)
71. Cao GZ, Metselaar R (1991) *Chem Mater* 3(2):242
72. Jama SAB, Thompson DP, Jack KH (1975) *Spec Ceram* 6:299
73. Hampshire S, Park HK, Thompson DP, Jack KH (1978) *Nature* 274(5674):880
74. Acikbas NC, Suvaci E, Mandal H (2006) *J Am Ceram Soc* 89(10):3255
75. Ekström T, Falk LKL, Shen ZJ (1997) *J Am Ceram Soc* 80(2):301
76. Soderlund E, Ekstrom T (1990) *J Mater Sci* 25(11):4815. doi:[10.1007/BF01129947](https://doi.org/10.1007/BF01129947)
77. Ekström T (1989) *Mater Sci Eng A* 109:341
78. Liu DM, Chen CJ, Lee RRR (1995) *J Appl Phys* 77(2):494
79. Hampshire S, Pomeroy MJ (2008) *Int J Appl Ceram Technol* 5(2):155
80. Çaliş N, Kuşhan ŞR, Kara F, Mandal H (2004) *J Eur Ceram Soc* 24(12):3387
81. Carruthers WD, Becher PF, Ferber MK, Pollinger J (2002) In: *Proceedings of ASME Turbo Expo, Amsterdam, 3–6 June 2002*
82. Shen ZJ, Peng H, Pettersson P, Nygren M (2002) *J Am Ceram Soc* 85(11):2876
83. Woodruff AK, Hellmann J (2006) In: *Technical Report ARL-CR-573, June 2006, Army Research Laboratory, Aberdeen Proving Ground*
84. Su XL, Wang PL, Chen WW, Zhu B, Cheng YB, Yan DS (2004) *J Am Ceram Soc* 87(4):730
85. Zalite I, Zilinska N, Kladler G (2007) *J Phys* 93(1):012008
86. Jack KH (1986) In: *Non-oxide technical and engineering ceramics, chapter sialons: a study in materials development. Elsevier Applied Science, London*
87. Kirby KW, Jankiewicz A, Janney M, Walls C, Kupp D (2000) In: *Proceedings of the 8th Department of defense electromagnetic windows symposium. U.S. Air Force Academy, Colorado Springs*
88. Hardie D, Jack KH (1957) *Nature* 180(4581):332
89. Grün R (1979) *Acta Crystallogr B* 35:800
90. Kuwabara Akihide, Matsunaga Katsuyuki, Tanaka Isao (2008) *Phys Rev B* 78(6):064104
91. Watari K, Hirao K, Brito ME, Toriyama M, Ishizaki K (2005) *Adv Technol Mater Mater Proc J* 7(2):191
92. Sukanuma K (1990) In: *Joining of ceramics, chapter joining silicon nitride to metals and to itself. Chapman and Hall, London*
93. Hayashi K, Tsujimoto S, Nishikawa T, Imamura Y (1986) *Adv Technol Mater Mater Proc J* 94(6):595
94. Zhou You, Zhu Xinwen, Hirao Kiyoshi, Lences Zoltan (2008) *Int J Appl Ceram Technol* 5(2):119
95. Lofaj Frantisek, Wiederhorn Sheldon N (2009) *J Ceram Proc Res* 10(3):269
96. Wiederhorn SM, Krause RF, Lofaj F, Taffner U (2005) In: Kim HD, Lin HT, Hoffmann MJ (eds) *Advanced Si-based ceramics and composites, vol 287 of Key Engineering Materials. Trans Tech Publications Ltd, Stafa-Zurich*
97. Ling G, Yang HT (2005) *Mater Chem Phys* 90(1):31
98. Dodd SP, Saunders GA, Cankurtaran M, James B (2001) *J Mater Sci* 36(3):723. doi:[10.1023/A:1004897126648](https://doi.org/10.1023/A:1004897126648)
99. Sosman RB (1927) In: *The properties of silica. American Chemical Society Monograph Series (No. 37), Book Department, The Chemical Catalog Company, Inc., New York*
100. Swab JJ, Wereszczak AA, Tice J, Caspe R, Kraft RH, Adams JW (2005) In: *Technical report ARL-TR-3417. Army Research Laboratory. Army Research Laboratory, Aberdeen Proving Ground*
101. Snead LL, Zinkle SJ, White DP (2005) *J Nucl Mater* 340(2–3):187
102. Bruls RJ, Hintzen HT, de With G, Metselaar R (2001) *J Eur Ceram Soc* 21(3):263
103. Kume S, Yasuoka Mi, Lee S-K, Kan A, Ogawa H, Watari K (2007) *J Eur Ceram Soc* 27(8–9):2967
104. De With G, Hattu N (1983) *J Mater Sci* 18(2):503. doi:[10.1007/BF00560639](https://doi.org/10.1007/BF00560639)
105. Toutanji HA, Friel D, El-Korchi T, Nathan KR, Wechsler G, Rafaniello W (1995) *J Eur Ceram Soc* 15(5):425
106. Fukuhara M, Sanpei A, Shibuki K (1997) *J Mater Sci* 32(5):1207. doi:[10.1023/A:1018583918380](https://doi.org/10.1023/A:1018583918380)
107. Daly BC, Antonelli GA, Maris HJ, Ford WK, Wong L, Andideh E (2002) *Phys B* 316:254
108. Heidinger R (2003) In: *Proceedings of the 22nd Symposium on fusion technology, vol 66–68. Fusion Engineering and Design, Helsinki*
109. Ye J, Kojima N, Furuya K, Munakata F, Okada A (2002) *J Therm Anal Calorim* 69(3):1031
110. Watari K, Hirao K, Toriyama M, Ishizaki K (1999) *J Am Ceram Soc* 82(3):777
111. Kumar A, Jayakumar T, Raj B, Ray KK (2003) *Acta Mater* 51(8):2417
112. Sirdeshmukh DB, Subhadra KG (2005) *J Mater Sci* 40(7):1553. doi:[10.1007/s10853-005-0654-3](https://doi.org/10.1007/s10853-005-0654-3)
113. Dean EA, Lopez JA (1983) *J Am Ceram Soc* 66(5):366
114. Phani KK, Niyogi SK (1987) *J Mater Sci* 22(1):257. doi:[10.1007/BF01160581](https://doi.org/10.1007/BF01160581)
115. Lam DCC, Lange FF, Evans AG (1994) *J Am Ceram Soc* 77(8):2113

116. Yoshimura HN, Molisani AL, Narita NE, Cesar PF, Goldenstein H (2007) *Mater Res* 10(2):127
117. Hasselman DPH (1962) *J Am Ceram Soc* 45(9):452
118. Knudsen FP (1959) *J Am Ceram Soc* 42(8):376
119. Morrell R (1985) *Handbook of properties of technical & engineering ceramics: part 1: an introduction for the engineer and designer*. Her Majesty's Stationary Office, London
120. Timoshenko SP, Goodier JN (1970) In: *Engineering societies monographs*, 3rd edn. McGraw-Hill, Singapore
121. Wright AF (1997) *J Appl Phys* 82(6):2833
122. Nye JF (1957) In: *Physical properties of crystals: their representation by tensors and matrices*. Clarendon Press, Oxford
123. Alers GA, Neighbours JR (1957) *J Appl Phys* 28(12):1514
124. Voigt W (1928) *Lehrbuch der Kristallphysik (mit Ausschluss der Kristalloptik)*. B. G. Teubner, Leipzig
125. Reuss A (1929) *Z Angew Math Mech* 9(1):49
126. Hill R (1952) *Proc Phys Soc Sect A* 65(5):349
127. Chung DH, Buessem WR (1967) *J Appl Phys* 38(6):2535
128. Wachtman JB, Tefft WE, Lam DG, Apstein CS (1961) *Phys Rev* 122(6):1754
129. Munro RG (2004) *J Res Nat Inst Stand Technol* 109(5):497
130. Anderson OL (1966) *Phys Rev* 144(2):553
131. Wachtman JB, Lam DG (1959) *J Am Ceram Soc* 42(5):254
132. Fukuhara M, Yamauchi I (1993) *J Mater Sci* 28(17):4681. doi: [10.1007/BF00414258](https://doi.org/10.1007/BF00414258)
133. Wolfenden A (1997) *J Mater Sci* 32(9):2275. doi: [10.1023/A:1018524200517](https://doi.org/10.1023/A:1018524200517)
134. Sánchez-González E, Miranda P, Meléndez-Martínez JJ, Guiberteau F, Pajares A (2007) *J Eur Ceram Soc* 27(11):3345
135. Staehler JM, Predebon WW, Pletka BJ, Subhash G (2000) *Mater Sci Eng A* 291(1–2):37
136. Unni CK, Gordon DE (1995) *J Mater Sci* 30(5):1173. doi: [10.1007/BF00356116](https://doi.org/10.1007/BF00356116)
137. McSkimin HJ (1953) *J Appl Phys* 24(8):988
138. McSkimin HJ (1959) *J Acoust Soc Am* 31(3):287
139. Fukuhara M, Sampei A (1999) *J Mater Sci Lett* 18(10):751
140. Carnevale EH, Larson GS, Lynnworth LC (1964) *J Acoust Soc Am* 36(9):1678
141. Wereszczak AA, Ferber MK, Jenkins MG, Lin CKJ, Breder K, Kirkland TP (1996) In: *Technical Report ORNL/TM-12943*, Oak Ridge National Laboratory, Oak Ridge
142. Xia Q, Xia H, Ruoff AL (1993) *J Appl Phys* 73(12):8198
143. Ueno M, Onodera A, Shimomura O, Takemura K (1992) *Phys Rev B* 45(17):10123
144. Peng Feng, Chen Dong, Fu Hongzhi, Cheng Xinlu (2008) *Phys B* 403(23–24):4259
145. Hazen RM, Finger LW (1986) *J Appl Phys* 59(11):3728
146. Cline CF, Stephens DR (1965) *J Appl Phys* 36(9):2869
147. Spinner S, Tefft WE (1961) In: *Proceedings ASTM*, Kansas City
148. Kipp ME, Grady DE (1994) *J Phys IV* 4(C8):249
149. Cline CF, Dunegan HL, Henderson GW (1967) *J Appl Phys* 38(4):1944
150. Rice RW (1997) *J Mater Sci* 32(12):3071. doi: [10.1023/A:1018630113180](https://doi.org/10.1023/A:1018630113180)
151. Koike J, Tashima S, Wakiya S, Maruyama K, Oikawa H (1996) *Mater Sci Eng* 220(1–2):26
152. Raiser GF, Wise JL, Clifton RJ, Grady DE, Cox DE (1994) *J Appl Phys* 75(8):3862
153. Mizuta H, Oda K, Shibasaki Y, Maeda M, Machida M, Ohshima K (1992) *J Am Ceram Soc* 75(2):469
154. Boch P, Glandus JC, Jarrige J, Lecompte JP, Mexmain J (1982) *Ceram Int* 8(1):34
155. Glandus JC, Besson JL, Boch P (1981) *Sci Ceram* 11:419
156. Terao R, Tatami J, Meguro T, Komeya K (2002) *J Eur Ceram Soc* 22(7):1051
157. Bentle GG, Kniefel RM (1965) *J Am Ceram Soc* 48(11):570
158. Jones MI, Hyuga H, Hirao K, Yamauchi Y (2004) *J Am Ceram Soc* 87(4):714
159. Chen IW, Rosenflanz A (1997) *Nature* 389(6652):701
160. Kim J, Rosenflanz A, Chen IW (2000) *J Am Ceram Soc* 83(7):1819
161. Hazelton C, Rice J, Snead LL, Zinkle SJ (1998) *J Nucl Mater* 253(1–3):190
162. Hatanaka K, Shiota H, Ando T (1991) *JSME (Jpn Soc Mech Eng) Int J Ser Solid Mech Mater* 34(3):351
163. Tennery VJ, Breder K, Ferber MK, Jenkins MG (2000) *J Am Ceram Soc* 83(5):1177
164. McLean AF, Hartsock DL (1989) In: *Wachtman JB (eds) Structural ceramics: treatise on materials science and technology*, vol 29. Academic Press, New York
165. Robards CF, Gangler JJ (March 2nd 1951) In: *Technical Report NACA Research Memorandum E50G21*, Lewis Flight Propulsion Laboratory, Cleveland
166. Tennery VJ, Breder K, Ferber MK, Jenkins MG (2000) *J Am Ceram Soc* 83(5):1186
167. Subhash G, Ravichandran G (1998) *J Mater Sci* 33(7):1933. doi: [10.1023/A:1004325926287](https://doi.org/10.1023/A:1004325926287)
168. Kelley KK (1960) In: *Technical report*, United States Department of the Interior, Bureau of Mines, Washington
169. Sergeev OA, Shashkov AG, Umanskii AS (1982) *J Eng Phys Thermophys* 43:1375
170. White GK, Minges ML (1997) *Int J Thermophys* 18(5):1269
171. Sedmidubský D, Leitner J (2006) *J Cryst Growth* 286(1):66
172. Kelley KK (1939) *J Am Chem Soc* 61(5):1217
173. Victor AC, Douglas TB (1963) *J Res Nat Bur Stand A* 67(4):325
174. Inaba H (1999) *J Phase Equilib* 20(3):187
175. Swindeman RW (1964) *J Nucl Mater* 14:404
176. Berman R (1976) *Thermal conduction in solids*. Clarendon Press, Oxford
177. Bruls RJ, Hintzen HT, Metselaar R (2005) *J Eur Ceram Soc* 25(6):767
178. Hirao K, Watari K, Brito ME, Toriyama M, Kanzaki S (1996) *J Am Ceram Soc* 79(9):2485
179. Drabble JR, Goldsmid HJ (1961) In: *Thermal conduction in semiconductors. International Series of Monographs on Semiconductors*, vol 4. Pergamon Press, Oxford
180. Abratis RJ, Dargis AK, Rusyatskas AA, Sakalauskas EJ (1999) *Refract Ind Ceram* 40(7–8):351
181. Kingery WD, Francl J, Coble RL, Vasilos T (1954) *J Am Ceram Soc* 37(2):107
182. AlShaikhiand A, Srivastava GP (2008) *J Appl Phys* 103(8):083554
183. Geith A, Kulig M, Hofmann T, Russel C (1993) *J Mater Sci* 28(4):865. doi: [10.1007/BF00400866](https://doi.org/10.1007/BF00400866)
184. AlShaikhi A, Srivastava GP (2007) *J Phys* 92(1):012084
185. Harris JH, Enck RC, Youngman RA (1993) *Phys Rev B* 47(9):5428
186. Sugawara A (1969) *Physica* 41(3):515
187. Haggerty JS, Lightfoot A (1995) *Ceram Eng Sci Proc* 16(4):475
188. Watari K, Li BC, Pottier L, Fournier D, Toriyama M (2000) In: *Murata, Shinozaki K, Kimura T (eds) Electroceramics in Japan III, vol 181-1 of Key Engineering Materials*, p 239. Trans Tech Publications Ltd, Zurich
189. Morelli DT, Heremans JP (2002) *Appl Phys Lett* 81(27):5126
190. Hirosaki N, Ogata S, Kocer C, Kitagawa H, Nakamura Y (2002) *Phys Rev B* 65(13):134110
191. Akimune Y, Munakata F, Matsuo K, Hirosaki N, Okamoto Y, Misono K (1999) *J Ceram Soc Jpn* 107(4):339
192. Watari K, Seki Y, Ishizaki K (1989) *J Ceram Soc Jpn* 97(1):56
193. Negita K (1985) *J Mater Sci Lett* 4(6):755
194. Hirosaki N, Okamoto Y, Ando M, Munakata F, Akimune Y (1996) *J Ceram Soc Jpn* 104(1):49

195. Watari K, Brito ME, Toriyama M, Ishizaki K, Cao S, Mori K (1999) *J Mater Sci Lett* 18(11):865
196. Li B, Pottier L, Roger JP, Fournier D, Watari K, Hirao K (1999) *J Eur Ceram Soc* 19(8):1631
197. Watari K, Hirao K, Brito ME, Toriyama M, Kanzaki S (1999) *J Mater Res* 14(4):1538
198. Hirosaki N, Okamoto Y, Ando M, Munakata F, Akimune Y (1996) *J Am Ceram Soc* 79(11):2878
199. Okamoto Y, Hirosaki N, Ando M, Munakata F, Akimune Y (1997) *J Ceram Soc Jpn* 105(7):631
200. Furuya K, Munakata F, Matsuo K, Akimune Y, Ye J, Okada A (2002) *J Therm Anal Calorim* 69(3):873
201. Zhu X, Zhou Y, Hirao K, Lences Z (2006) *J Am Ceram Soc* 89(11):3331
202. Okamoto Y, Hirosaki N, Ando M, Munakata F, Akimune Y (1998) *J Mater Res* 13(12):3473
203. Hirosaki N, Ando M, Okamoto Y, Munakata F, Akimune Y, Hirao K, Watari K, Brito ME, Toriyama M, Kanzaki S (1996) *J Ceram Soc Jpn* 104(12):1171
204. Akimune Y, Munakata F, Matsuo K, Okamoto Y, Hirosaki N, Satoh C (1999) *J Ceram Soc Jpn* 107(12):1180
205. Hirosaki N, Okamoto Y, Munakata F, Akimune Y (1999) *J Eur Ceram Soc* 19(12):2183
206. Lee SK, Moretti JD, Readey MJ, Lawn BR (2002) *J Am Ceram Soc* 85(1):279
207. Hayashi H, Hirao K, Yamauchi Y, Kanzaki S (March 24 2003) In: Annual meeting of the ceramic society of Japan, Tokyo
208. Abdulagatov IM, Emirov SN, Tsomaeva TA, Gairbekov KA, Askerov SY, Magomedova NA (2000) *J Phys Chem Solids* 61(5):779
209. Han I-S, Seo D-W, Kim S-Y, Hong K-S, Guahk KH, Lee KS (2008) *J Eur Ceram Soc* 28(5):1057
210. Slack Glen A, Bartram SF (1975) *J Appl Phys* 46(1):89
211. Iwanaga H, Kunishige A, Takeuchi S (2000) *J Mater Sci* 35(10):2451. doi:[10.1023/A:1004709500331](https://doi.org/10.1023/A:1004709500331)
212. Walker DG, Mayer RM, Hickman BS (1964) *J Nucl Mater* 14:147